

LSD: Lyman-break galaxies Stellar populations and Dynamics. I: Mass, metallicity and gas at $z \sim 3.1$ *

F. Mannucci¹†, G. Cresci^{1,2}, R. Maiolino³, A. Marconi⁴, G. Pastorini⁴, L. Pozzetti⁵, A. Gnerucci⁴, G. Risaliti^{1,6}, R. Schneider¹, M. Lehnert⁷, & M. Salvati¹

¹INAF - Osservatorio Astrofisico di Arcetri, Largo E. Fermi 5, I-50125, Firenze, Italy

²Max-Planck-Institut für extraterrestrische Physik (MPE), Giessenbachstr.1, D-85748 Garching, Germany

³INAF - Osservatorio Astronomico di Roma, via di Frascati 33, I-00040 Monte Porzio Catone, Italy

⁴Dip. di Astronomia e Scienza dello Spazio, Università di Firenze, Largo E. Fermi 2, I-50125, Firenze, Italy

⁵INAF - Osservatorio Astronomico di Bologna - Via Ranzani,1, I-40127, Bologna, Italy

⁶Harvard-Smithsonian Center for Astrophysics, 60 Garden Street, Cambridge, MA 02138, USA

⁷GEPI, Observatoire de Paris, CNRS, University Paris Diderot, 5 Place Jules Janssen, F-92190 Meudon, France

Submitted 2009 February

ABSTRACT

We present the first results of a project, LSD, aimed at obtaining spatially-resolved, near-infrared spectroscopy of a complete sample of Lyman-Break Galaxies at $z \sim 3$. Deep observations with adaptive optics resulted in the detection of the main optical lines, such as [OII] λ 3727, H β , and [OIII] λ 5007, which are used to study sizes, SFRs, morphologies, gas-phase metallicities, gas fractions and effective yields. Optical, near-IR and Spitzer/IRAC photometry is used to measure stellar mass. We obtain that morphologies are usually complex, with the presence of several peaks of emissions and companions that are not detected in broad-band images. Typical metallicities are 10–50% solar, with a strong evolution of the mass-metallicity relation from lower redshifts. Stellar masses, gas fraction, and evolutionary stages vary significantly among the galaxies, with less massive galaxies showing larger fractions of gas. In contrast with observations in the local universe, effective yields decrease with stellar mass and reach solar values at the low-mass end of the sample. This effect can be reproduced by gas infall with rates of the order of the SFRs. Outflows are present but are not needed to explain the mass-metallicity relation. We conclude that a large fraction of these galaxies are actively creating stars after major episodes of gas infall or merging.

Key words: Galaxies: abundances; Galaxies: formation; Galaxies: high-redshift; Galaxies: starburst

1 INTRODUCTION

Metallicity is one of the most important properties of galaxies, and its study is able to shed light on the details of galaxy formation. It is an integrated property, not related to the present level of star formation, but rather to the whole past history of the galaxy. In particular, metallicity is sensitive to the fraction of baryonic mass already converted into stars, i.e., to the evolutionary stage of the galaxy. Also, metallicity is affected by the presence of infalls and outflows, i.e., by

feedback processes and by the interplay between the forming galaxy and the intergalactic medium.

The existence of a clear correlation between luminosity and metallicity of galaxies is known from the late '70s (Lequeux et al. 1979). It is now clear that local galaxies follow a well-defined mass-metallicity relation, where galaxies with larger stellar mass or larger circular velocity have higher metallicities (Garnett 2002; Pérez-González et al. 2003; Pilyugin et al. 2004; Tremonti et al. 2004; Lee et al. 2006; Panter et al. 2008; Kewley & Ellison 2008; Hayashi et al. 2008; Michel-Dansac et al. 2008; Liu et al. 2008). The origin of the relation is uncertain because several effects can be, and probably are, active. It is well known that, in the local universe, starburst galaxies eject a significant amount of metal-enriched gas into the intergalactic medium because of energetic feedback from exploding SNe (see, for

* Based on observations collected with ESO/VLT (proposals 075.A-0300 and 076.A-0711), with the Italian TNG, operated by FGG (INAF) at the Spanish Observatorio del Roque de los Muchachos, and with the Spitzer Space Telescope, operated by JPL (Caltech) under a contract with NASA.
† E-mail: filippo@arcetri.astro.it

example, Lehnert & Heckman 1996a; Mori et al. 2004 and Scannapieco et al. 2008, and references therein). Numerous studies have shown that outflows are already present at high redshifts (Pettini et al. 2001, 2002; Frye et al. 2002; Weiner et al. 2008). Outflows are expected to be more important in low-mass galaxies, where the gravitational potential is lower and a smaller fraction of gas is retained. As a consequence, higher mass galaxies are expected to be more metal rich (see, for example, Edmunds 1990 and Garnett 2002).

A second possible effect shaping the mass-metallicity relation is related to the well known effect of “downsizing” (e.g., Gavazzi & Scodreggio 1996; Cowie et al. 1996), i.e., lower-mass galaxies form their stars later and on longer time scales than more massive systems. At a given time, lower mass galaxies have formed a smaller fraction of their stars, therefore are expected to show lower metallicities (Ellison et al. 2008). Recently, Calura et al. (2009) have explained the evolution of the mass-metallicity relation up to $z=3.5$ as due to an increase of the efficiency of star formation with galaxy mass, without invoking differential galactic outflows.

Other possibilities exist, for example some properties of star formation, as the initial mass function (IMF), could change systematically with galaxy mass (Köppen et al. 2007).

All these effects have a deep impact on galaxy evolution, and the knowledge of their relative contributions is of crucial importance. Different models have been built to reproduce the shape of the mass-metallicity relation in the local universe, and different assumptions produce divergent predictions at high redshifts ($z > 2$). It is possible to test these predictions as metallicities can now be measured at high redshifts (Kobulnicky & Koo 2000; Pettini et al. 2001, 2002; Maier et al. 2006). To explore this issue several groups have observed the mass-metallicity relation in the distant universe, around $z=0.7$ (Savaglio et al. 2005; Rodrigues et al. 2008), between 0 and 1.5 (Cowie & Barger 2008) between 0.5 and 1.2 (Lamareille et al. 2008; Perez-Montero et al. 2008), and at $z\sim 2$ (Erb et al. 2006a; Halliday et al. 2008; Hayashi et al. 2008). They have found a clear evolution with cosmic time, with metallicity decreasing with increasing redshift, for a given stellar mass. Erb et al. (2006a,b) used near-IR long-slit spectra of a large number of LBGs at $z\sim 2$ to estimate the average amount of extinction and estimate the intrinsic star formation rate (SFR). By assuming that the Schmidt law holds at $z=2$ (see below), they also derive the fraction of baryonic mass in gas, and measure the effective yields.

There are several reasons to explore even higher redshifts. The redshift range at $z\sim 3-4$ is particularly interesting: it is before the peak of the cosmic star formation density (see, for example, Hopkins & Beacom 2006; Mannucci et al. 2007), only a small fraction ($\sim 15\%$, Pozzetti et al. 2007) of the total stellar mass (M_*) has already been created, is the redshift range where the most massive early-type galaxies are expected to form (see, for example, Saracco et al. 2003), the number of mergers among the galaxies is much larger than at later times (Conselice et al. 2007; Stewart et al. 2008). As a consequence, it is above $z\sim 3$ that predictions of different models tend to diverge significantly, and it is im-

portant to sample this redshift range observationally. The observations are really challenging because of the faintness of the targets and the precision required to obtain a reliable metallicity. Nevertheless, the new integral-field unit (IFU) instruments on 8-m class telescopes are sensitive enough to allow for the project.

Metallicity at $z\sim 3$ can be obtained by measuring the fluxes of the main optical emission lines ($[\text{OII}]\lambda 3727$, $\text{H}\beta$, $[\text{OIII}]\lambda 5007$, $\text{H}\alpha$), whose ratios have been calibrated against metallicity in the local universe (Nagao et al. 2006; Kewley & Ellison 2008 and references therein). Of course, this method can be applied only to line-emitting galaxies, i.e., to low-extinction, star-forming galaxies, whose lines can be observed even at high-redshifts (e.g., Teplitz et al. 2000; Pettini et al. 2001, 2002; Erb et al. 2006a). In contrast, the gas metallicity of more quiescent and/or dust extinguished galaxies, like Extremely Red Galaxies (EROs, Mannucci et al. 2002), Distant Red Galaxies (DRGs, Franx et al. 2003), and Sub-mm Galaxies (SMGs, Chapman et al. 2005), cannot be easily measured at high redshifts. Stellar metallicities, revealed by absorption lines, can also be measured (Gallazzi et al. 2006; Panter et al. 2008; Halliday et al. 2008), but at $z > 3$ this is even more observationally challenging.

Together with metallicity, the dynamical properties of galaxies have a special role for their understanding. Dynamics is directly related to the models of galaxy formation and it is the most direct way to probe the content of dark matter.

Not much is known about dynamics of high redshift galaxies as high-resolution, high-sensitivity, spectroscopic observations are required. Nesvadba et al. (2006) and Stark et al. (2008) observed highly lensed LBGs at $z\sim 3.1$ to obtain the velocity field. In these cases, the high spatial resolution on the source plane is provided by the presence of the gravitational lens, distorting the galaxy and stretching its apparent dimensions to several arcsecs. Nesvadba et al. (2006) found rotation velocities of 75 km/sec within the central lens-corrected 0.5 kpc, revealing the presence of a dynamical mass $\log(M/M_\odot)=9.3$. Stark et al. (2008) found a well ordered source, similar to local spirals. Förster Schreiber et al. (2006) obtained seeing-limited near-IR integral field spectroscopy of a large sample of galaxies at $z\sim 2$. A significant fraction of this composite sample of spatially extended, $\text{H}\alpha$ -emitting galaxies shows dynamical properties consistent with being the precursor of normal disk galaxies in the local universe. Other recent works by Bouché et al. (2007), Genzel et al. (2008) and Cresci et al. (2009) are addressing this problem, and the amount of accumulated information is rapidly growing.

Aimed at studying the high-redshift metallicity and dynamics, we started two projects, AMAZE (Assessing the Mass-Abundance redshift Evolution) and LSD (Lyman-break galaxies Stellar populations and Dynamics)¹. For both projects we observed a sample of galaxies at $z=3-4$ with an IFU 3D spectrograph in order to derive their chemical and dynamical properties. 3D spectroscopy is a key technique

¹ This acronym is not to be confused with two others often used by astronomers, one of which is “Lens Structure and Dynamics” by Koopmans & Treu (2003).

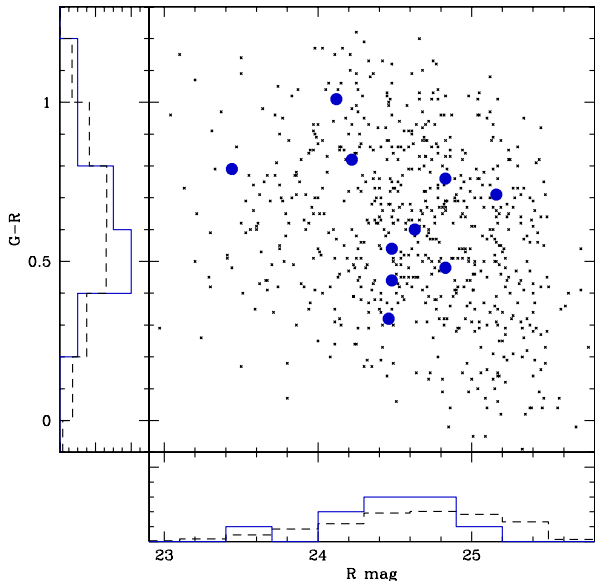


Figure 1. Distribution in R magnitude and (G–R) color of the LSD targets (solid blue dots) compared to the spectroscopically confirmed targets of the Steidel et al. (2003) sample with $2.5 < z < 3.3$ (small dots). The solid blue histograms show the distributions of these quantities for the LSD sample, which are similar to those for the total parent sample (dashed histograms).

for these studies as it allows to derive the full velocity field of the galaxies, without the need to restrict the study to a slit. Also, integrated spectra of the galaxies can be obtained without slit losses. This is particularly important when the flux ratios between lines at different wavelengths are derived, as differential losses can spoil the results.

For AMAZE, described in Maiolino et al. (2008), we selected 30 galaxies with deep Spitzer/IRAC photometry ($3.6\text{--}8\ \mu\text{m}$), an important piece of information to derive a reliable stellar mass. These galaxies were observed, in seeing-limited mode, with the IFU spectrometer SINFONI on ESO/VLT.

The aim of LSD is not only to measure metallicities, but also to obtain spatially-resolved spectra to measure dynamics and spectral gradients. For this reason we used adaptive optics to improve the spatial resolution. Also, we selected a complete, albeit small, sample of LBGs, in order to obtain results that can be applied to the LBG population as a whole. This is the first paper about LSD, focusing on the chemical properties, while the dynamical properties will be examined in a forthcoming paper.

In the following, we adopt a Λ CDM cosmology with $H_0 = 70$ km/sec, $\Omega_m = 0.3$ and $\Omega_\Lambda = 0.7$. At $z = 3.1$, the universe is 2 Gyr old, 15% of its current age.

2 SAMPLE SELECTION

Our sample of LBGs was extracted from the Steidel et al. (2003) catalog, which contains about 1000 spectroscopically-confirmed LBGs, selected in 17 fields down to a limiting magnitude of $R_{AB} = 25.5$. The parent catalog was searched for the presence of bright stars ($R < 15$) within $\sim 35''$ of each

source, resulting in the selection of ~ 100 sources. The presence of a bright foreground star is needed to drive the adaptive optics module and obtain a resolution comparable with the diffraction limit of a 8m class telescope, about $0.1''$ in the near-IR. The best combinations of star brightness and distance from the target were selected to obtain the final sample of 10 objects presented in Table 1.

We emphasize that no other property was used to select the targets, thus the present sample, albeit small, should be representative of the LBG population in the Steidel et al. (2003) sample. This is shown in figure 1, which compares the distributions of R-band magnitude and (G–R) color of the selected targets with those of the parent population of LBGs. The distributions of both quantities are similar, with no apparent biases.

In order to check the possible presence of Active Galactic Nuclei, we inspected the available X-ray observations of these galaxies. For two objects, DSF2237b-D28 and DSF2237b-MD19, no X-ray observation is available. The other sources lay in the field of a deep *Chandra* observation (SSA22) and in that of a quasar observed with *XMM-Newton*. No source is detected in the 0.5–10 keV range. In all cases, the off-center position of the sources, and/or the short exposure time imply a relatively high upper limit for the X-ray flux, which, given the high redshift of the sources, corresponds to X-ray luminosities larger than $\sim 10^{43}$ erg s^{-1} . Although these limits cannot rule out the presence of an AGN, there is no direct evidence for it. In all cases we can exclude a dominant, quasar-like AGN contribution.

3 OBSERVATIONS AND DATA REDUCTION

The selected objects have been observed with several instruments in order to obtain a complete data set.

3.1 Integral field spectroscopy

The targets were observed at ESO/VLT by using the SINFONI instrument (Eisenhauer et al. 2003; Bonnet et al. 2004), an IFU spectrograph fed by an adaptive optics module with a Natural Guide Star (NGS). The IFU splits the incoming light into several adjacent slits, and a spectrum is obtained for each location in the field-of-view. Several spatial scales are available, corresponding to different spatial resolutions. For 8 of the 10 targets we used the 50×100 mas/pixel scale, providing a field-of-view of $3'' \times 3''$. Such a scale is a good match of the theoretical diffraction limit in the K-band on the VLT telescope, which is ~ 70 mas, and the field-of-view is appropriate to observe galaxies of dimensions of $\sim 1''$. Two objects constitute a pair of interacting galaxies at a distance of about $2''$, in this case we used a larger scale, 125×250 mas/pixels with a total field-of-view of $8'' \times 8''$.

In all cases we used the H+K grating, providing a simultaneous coverage of these two near-IR bands ($1.5\text{--}2.4\ \mu\text{m}$), with resolution $\lambda/\Delta\lambda \sim 1400$ in the H band and ~ 1800 in the K band.

Observations were divided into independent sequences of about 45 min each, due to the limitation of the ESO service observing strategy based on observing blocks (OBs) of about 1 hour of total time. During each OB, an ABBA nodding was used, putting the target in two positions of the

Table 1. Target list and summary of the observations

(1) Object	(2) R.A. (J2000)	(3) Dec.	(4) R_{AB}	(5) z_{em}	(6) Dist	(7) R mag	(8) SINFONI Scale	(9) Texp	(10) T(1+3)	(11) SPITZER T(2+4)	(12) N/A
SSA22a-C30	22:17:19.3	+00:15:44.7	24.2	3.103	35''	13.0	50×100	240	50	50	A
SSA22a-C6	22:17:40.9	+00:11:26.0	23.4	3.097	35''	12.0	125×250	280	83	133	N
SSA22a-M4	22:17:40.9	+00:11:27.9	24.8	3.098	35''	12.0	125×250	280	83	133	N
SSA22b-C5	22:17:47.1	+00:04:25.7	25.2	3.112	11''	14.9	50×100	240	83	133	N
DSF2237b-D28	22:39:20.2	+11 55 11.3	24.5	2.933	26''	13.1	50×100	240	96	96	A
DSF2237b-MD19	22:39:21.1	+11 48 27.7	24.5	2.611	20''	14.1	50×100	200	-	-	-
Q0302-C131	03:04:35.0	-00:11:18.3	24.5	3.235	26''	13.4	50×100	240	332	133	N
Q0302-M80	03:04:45.7	-00:13:40.6	24.1	3.414	15''	14.5	50×100	240	166	399	N
Q0302-C171	03:04:44.3	-00:08:23.2	24.6	3.328	33''	14.6	50×100	240	332	-	N
Q0302-MD287	03:04:52.8	-00:09:54.6	24.8	2.395	13''	15.0	50×100	160	249	-	N

Columns: (1-3): Target name and coordinates; (4): Target R-band magnitude; (5): Redshift from emission lines; (6-7): Guide star distance and R-band magnitude; (8-9): spatial scale (mas) and total exposure time (min) of the SINFONI observations; (10-11): exposure time (min) for Spitzer/IRAC observations in channels 1+3 and 2+4; (12) New (N) or Archive (A) Spitzer/IRAC data.

field-of-view about $1.5''$ apart. This is a very efficient way to observe compact objects as no time is lost in observing the sky. Nevertheless, in principle this could introduce some self-subtraction of the wings of the targets more extended than $1.5''$.

A maximum seeing of $0.8''$ was requested to carry out the observations, and an image of the reference star was observed at the beginning of each OB to monitor the conditions of the atmosphere during the observations.

Data were reduced by using the ESO pipeline (Modigliani et al. 2007) with the improved sky subtraction described by Davies (2007). After flat-fielding, sky-subtraction, correction for distortions and wavelength calibration, the 2D data of each OB are mapped into a 3D data cube with dimensions $32 \times 64 \times 2048$ pixels. The cubes of the different OBs are then combined together by measuring the relative offsets from the detected centroid of emission. We note that using the coordinates in the image header often does not provide the requested precision ($<0.1''$), as the measured pointing uncertainties are of the order of $0.2''$.

3.2 Photometric and morphological data

The original dataset of optical photometry in the UGR bands by Steidel et al. (2003) is available for all the objects. Such a limited wavelength range does not allow to obtain reliable stellar masses by fitting the spectral energy distribution (SED). The optical data must be complemented by near-IR photometry. J and K-band photometry of 4 objects was published by Shapley et al. (2001). We have observed the remaining 6 objects in the J and Ks filters with the NICS camera (Baffa et al. 2001) on the Italian 3.6m telescope TNG. Exposure times of 1–1.5 hours in J and 2–3.5 hours in Ks were used, according to the expected near-IR magnitudes. NICS data were reduced by the automatic pipeline SNAP².

Photometry at longer wavelengths ($3.6\text{--}8\mu\text{m}$) is available in the Spitzer/IRAC archive (Werner et al. 2004;

Fazio et al. 2004) for some of the objects in the SSA22 field. For the remaining objects we obtained targeted observation with Spitzer/IRAC during cycle 7, as listed in Table 1. We used the post-BSD products of the pipeline, and measured aperture photometry.

Finally, HST will observe these objects after SM4, both in the optical with ACS and in the near-IR with WFC3, providing accurate photometry and broad-band morphologies. In conclusion, these objects will have a complete set of photometric and spectroscopic observations with detailed morphological information at optical and near-IR bands, and will be suitable for detailed studies.

4 RESULTS AND MEASURED QUANTITIES

4.1 The detected lines

The final SINFONI data cubes were searched for the position of the brightest lines, either $[\text{OIII}]\lambda 5007$ or $\text{H}\alpha$, to define the spatial position of the target. The main optical lines ($[\text{OII}]\lambda 3727$, $\text{H}\beta$, $[\text{OIII}]\lambda 5007$ and $\text{H}\alpha$) are detected in 9 out of 10 galaxies, the only exception being Q0302-MD287. The reasons for this non detection are not clear. It is possible that its emission lines fall below our detection threshold, or that they coincide with bright sky lines. The SED fitting described in sect. 4.3 points toward the existence of a large amount of dust in this object, with A_V between 0.9 and 1.1 mag. As a consequence, it is also possible that the optical lines are not detected because of the presence of large amount of dust extinction.

The choice of the aperture for the extraction of the spectra is a important step. Measuring metallicity requires a good knowledge of line ratios, which are best obtained inside small apertures on the central regions of the galaxies, where the signal-to-noise is higher. In contrast, measuring total SFRs requires larger apertures to maximize the fraction of line emission recovered by aperture photometry. To measure all these quantities, we extracted complete spectra inside a circular aperture of $0.35''$ of diameter, corresponding to 7 pixels, and an aperture correction for a point source was applied to recover the emitted flux of the central part of

² <http://www.arcetri.astro.it/~filippo/snap>

Table 2. Properties of the detected lines

(1) Object	(2) line	(3) z	(4) Flux ^(a)	(5) Fact ^(b)
SSA22a-C30	[OII]3727	3.1024	0.30 ± 0.12	3.18
	H β	3.1030	0.26 ± 0.10	
	[OIII]4958	3.1034	0.34 ± 0.10	
	[OIII]5007	3.1026	1.28 ± 0.22	
SSA22a-C6	[OII]3727	3.0966	1.21 ± 0.38	1.09
	H β	3.0970	0.76 ± 0.45	
	[OIII]4958	3.0966	2.26 ± 0.78	
	[OIII]5007	3.0968	5.50 ± 0.62	
SSA22a-M4	[OII]3727	3.0961	1.46 ± 0.23	1.06
	H β	3.0976	0.69 ± 0.25	
	[OIII]4958	3.0965	1.08 ± 0.30	
	[OIII]5007	3.0978	3.66 ± 0.49	
SSA22b-C5	[NeIII]3869	3.1098	0.38 ± 0.14	1.57
	H β	3.1122	0.50 ± 0.14	
	[OIII]4958	3.1120	1.01 ± 0.22	
	[OIII]5007	3.1121	3.28 ± 0.24	
D2237b-D28	[OII]3727	2.9352	0.74 ± 0.16	1.84
	[OIII]4958	2.9328	0.50 ± 0.16	
	[OIII]5007	2.9324	1.86 ± 0.36	
D2237b-MD19	H β	2.6093	0.60 ± 0.16	1.95
	H α	2.6108	2.96 ± 0.46	
Q0302-C131	[OII]3727	3.2349	0.80 ± 0.32	1.29
	H β	3.2346	0.46 ± 0.16	
	[OIII]4958	3.2341	0.90 ± 0.20	
	[OIII]5007	3.2346	2.62 ± 0.52	
Q0302-M80	[OII]3727	3.4136	0.56 ± 0.18	1.23
	H β	3.4138	0.40 ± 0.12	
	[OIII]4958	3.3990	0.42 ± 0.20	
	[OIII]5007	3.4137	1.32 ± 0.26	
Q0302-C171	[OII] λ 3727	3.3287	0.56 ± 0.24	1.92
	H β	3.3289	0.18 ± 0.08	
	[OIII] λ 4958	3.3280	0.28 ± 0.08	
	[OIII] λ 5007	3.3279	1.10 ± 0.12	

Columns. (4): line flux inside an aperture of $0.35''$ with correction for the PSF, units of $10^{-17} \text{erg cm}^{-2} \text{sec}^{-1}$; (5): scaling factor to total flux

the galaxies. We chose a circular aperture, instead of more complex apertures based on object morphology and surface brightness, in order to avoid any problem with possible variations of the PSF with wavelength and a non perfect spatial alignment of the spectra. The fraction of total flux recovered by this procedure was estimated by computing the curve of grow of the photometry of the brightest line as a function of aperture radius. A correction for the missing flux is applied when the “total” quantities are needed. The results are shown in Table 2, listing the line fluxes inside the circular aperture and the correcting factor to total fluxes. Except for one galaxy, SSA22a-C30, composed by several clumps of emission, for all the other galaxies the tabulated fluxes comprise more than half of the total flux.

4.2 Morphologies and sizes

Fig. 2 shows the images of all the targets. Most of the galaxies show a sharp peak of line emission and some extended structure. In several cases, the objects appear to be composed by several clumps of emission. The distance between clumps is usually comparable to the dimension of the objects as revealed by ground-based imaging. In a few cases the distribution of the secondary peaks follow the continuum light, while in some cases we detected faint “companions” that are not detected in broad-band. VLT has a small pointing error, of the order of $0.2''$, but, compared to our resolution, this is enough to introduce a significant uncertainty in the relative astrometry between UV and line images. As a consequence, we cannot be sure where the line emission originates with respect to the UV image. Assuming that the main peak of line emission corresponds to the maximum of the UV light, the line-emission “companions” could be both secondary peak of star formation and line emission inside a single formed galaxy, or the signature of an ongoing merging. A detailed comparison with broad-band, rest-frame-UV morphology will be given on the basis of future HST images.

Images obtained with a NGS usually have a non-circular PSF (see, for example, Cresci et al. 2005). Increasing the distance of the scientific target from the NGS, the PSF becomes larger. The variation in the radial direction, i.e., towards the NGS, is larger than in the tangential direction. As a result, when this effect is dominant, the objects appear to be elongated toward the NGS. The magnitude of the effect depends on the conditions of the atmosphere and on the distance of the target from the NGS, and is of the order of $0.1''$ – $0.3''$. In our images, elongation toward the NGS is seen only in one case, meaning that in most cases the atmospheric conditions were good enough for AO observations and the isoplanatic angle in the K band was not significantly smaller than the separation between the target and the guide star.

No bright point sources are present in our field-of-view, preventing us from measuring the final PSF on the combined data themselves. To estimate the PSF we used the on-axis image of the NGS taken every hour at the beginning of each OB. The on-axis PSF FWHM was degraded to take into account the distance of the target galaxy from the NGS. For this we used the recipes in Cresci et al. (2005), using the values of the isoplanatic angle provided by the ESO database, and averaging over the different values obtained for the different OBs. As the seeing was always comprised in the narrow range 0.6 – $1.0''$ FWHM, no large differences are seen in most of the OBs. In all cases we obtained values of the PSF FWHM of the order of $0.2''$ for the fields observed with the smallest spatial scale, and $0.3''$ for the fields with the largest scale. These values are in good agreement with the results of the simulations provided by ESO, and were used in the following analysis.

Galaxy sizes have been estimated by fitting a Moffat function to the image in the brightest line, and the results have been deconvolved for the PSF. The measured half-light radii are listed in Table 3. Large uncertainties on the resulting sizes are present, both because images usually have low signal-to-noise ratio (SNR) and because the PSF

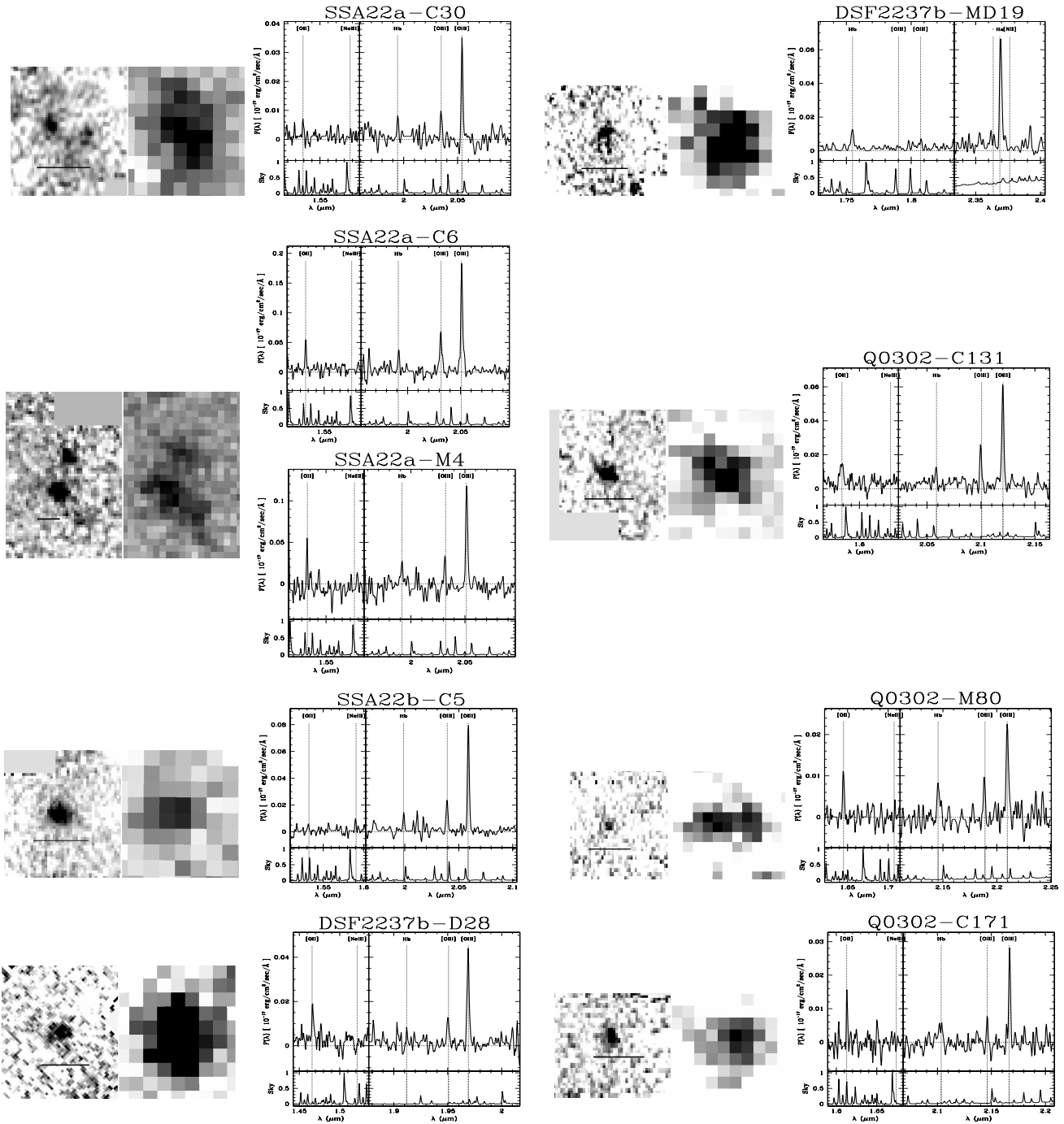


Figure 2. Images and spectra of the targets. For each object we show, from left to right: morphology in the emission line ($H\alpha$ for MD19, $[OIII]\lambda 5007$ for the others), ground-based R-band image by Steidel et al. (2003), and galaxy spectrum compared to the sky spectrum. The horizontal bars in the line images are $1''$ long. First column, from top to bottom: SSA22a-C30, the interacting system composed by SSA22a-C6 (south, upper spectrum) and SSA22a-M4 (north, lower spectrum), SSA22b-C5, DSF2237b-D28. Second column: DSF2237b-MD19, Q0302-C131, Q0302-M80 and Q0302-C171.

is not accurately known. Also, companions and secondary peaks of emission are not considered in measuring the dimensions. As this is also true for line fluxes, the derived metallicities (section 4.6) and gas mass (section 6.3), are consistently derived from the main peak only.

Since we are observing faint galaxies with high-spatial

resolution, surface brightness is probably our limiting factor. The dimensions of the detected line-emitting regions are sometimes significantly smaller than the dimensions obtained in the UV by ground-based imaging, even taking into account the larger PSF. They are also smaller than object sizes obtained with SINFONI/VLT without the use of AO by the Spectroscopic Imaging survey in the Near-infrared with

SINFONI (SINS) (Förster Schreiber et al. 2006, although at $z \sim 2.2$) and AMAZE (Maiolino et al. 2008) collaborations. We interpret these results as evidence that our detected sizes are indeed limited by surface brightness. The average limiting surface brightness is 1.2×10^{-16} erg/cm²/sec/arcsec². Such a sensitivity can be translated into a limiting SFR density at $z \sim 3.1$ detected with an emission line. For H β , the limiting SFR density is $\sim 4/M_{\odot}/\text{yr}/\text{kpc}^2$; for [OIII] $\lambda 5007$, assuming an average ratio of [OIII] $\lambda 5007$ /H β =4, the minimum detectable SFR density is $\sim 1M_{\odot}/\text{yr}/\text{kpc}^2$. This is similar to the SFR density at $z=2.2$ in Erb et al. (2006c), and it is adequate to detect a significant fraction of the local starbursts (Kennicutt 1998). Nevertheless, the outer, low surface brightness parts of these galaxies are probably lost in the noise, and morphologies could appear more compact than they actually are.

The measured half-light radii range between 0.7 and 2.4 kpc, with a median value of 1.36 kpc. These radii are similar to those in the sample of local starbursts in Lehnert & Heckman (1996b), who measure a median value of 1.70 kpc. Considering that our observations are less sensitive to the outer parts of the galaxies than Lehnert & Heckman (1996a), we conclude that LBGs tend to be as extended as local starbursts.

4.3 The Stellar mass

Stellar masses (M_*) are derived by fitting the SED with *Hyperzmass* (Pozzetti et al. 2007), a modified version of the photometric redshift code *Hyperz* (Bolzonella et al. 2000). These fits also provide estimates of age, current SFR and dust extinction of the dominant stellar population. The presence of good IRAC photometry allows the determination of reliable M_* as the SED is sampled up to the rest-frame J band. We have used the Bruzual & Charlot (2003) spectrophotometric models of galaxy evolution and smooth exponentially decreasing SFHs, constraining the age to be smaller than the Hubble time at galaxy redshift, as detailed in Pozzetti et al. (2007).

The photometric stellar masses have typical dispersions due to statistical uncertainties and degeneracies of the order of 0.2 dex. Metallicity has little influence on the SED, with uncertainties of ~ 0.05 dex, and we have set it to $Z=0.2 Z_{\odot}$, in agreement with what derived from the emission lines as described below. The addition of secondary bursts to a continuous star formation history produces systematically higher (up to 40% on average) stellar masses, while population synthesis models with TP-AGB phase (Maraston 2005) produce a systematic shift of ~ 0.1 dex towards lower M_* . Finally, the uncertainty on the absolute value of the M_* due to the assumptions on the IMF is within a factor of 2 for the typical IMFs usually adopted in the literature. We have used the Chabrier (2003) IMF with lower and upper cutoffs of 0.1 and 100 M_{\odot} . The resulting stellar masses can be scaled to the standard Salpeter IMF by multiplying them by a factor of 1.7 (Pozzetti et al. 2007).

The results are shown in Table 3. The listed errors are due to both statistical uncertainties and degeneracies. Masses, expressed in $\log(M_*/M_{\odot})$, range from 8.96 to 10.33, with a log average of 9.82. These values are consistent with those derived by Shapley et al. (2001) for their sample of LBGs at $z \sim 3$, averaging at 10.05 when converting their val-

ues to our IMF. Lower redshift BM/BX galaxies in the $z \sim 2$ sample of Erb et al. (2006b) are also quite similar, with an average $\log(M_*/M_{\odot})$ of 10.22, within ~ 0.3 of our average value.

Galaxy age, current SFR and dust extinction on the continuum $A_{V,c}$ cannot be individually well constrained because they suffer of significant degeneracy. The errors associated to each of these three quantities are large, and this is particularly important for extinction which is used to estimate the total SFR from emission lines. The range of the allowed values of $A_{V,c}$ is shown in Table 3. Despite the large errors, a possible correlation is seen between stellar mass and age, i.e., less massive galaxies are best-fitted by younger templates. The best-fitting age is of the order of $10^{7.5}$ yr for the less massive galaxies, and about 10^9 yr for the most massive ones.

4.4 Photoionization conditions

The values of SFR and metallicity derived in the next sections are correct only if the optical line emission is dominated by star formation and the conditions are not too different from those in the local universe. Even if the observed line ratios are typical of starburst galaxies, several problems could be present.

The first concern is that the presence of an AGN could alter line ratios and produce a spurious value of the inferred metallicity. No evidence of AGN is seen in the emission line shape, where the width of the forbidden lines is consistent with those of the permitted lines. This excludes the presence of a dominant broad-line AGN, but it does not help in excluding a narrow-line AGN (see the discussion in sec. 2).

The second concern is that significant differences in the conditions of star forming regions can be present, as LBGs at $z \sim 3$ have larger SFRs than most galaxies in the local universe. In particular, any evolution of the photoionization conditions could mimic a change of metallicity. The presence of evolution can be studied by comparing the flux ratios [NII]/H α vs. [OIII]/H β , and several studies at lower redshift indicate that such an evolution actually exists (Shapley et al. 2005; Erb et al. 2006a; Brinchmann et al. 2008; Liu et al. 2008). Line ratios discrepant from the local relation are often associated with higher SFR surface densities, interstellar pressures, and ionization parameters.

We have verified that all the observed line ratios are fully consistent with excitation from hot stars, but we cannot study the presence of evolution because in most cases we cannot observe H α . Nevertheless, several authors (Brinchmann et al. 2008; Liu et al. 2008) conclude that the influence of different ionization conditions on the derived metallicities is likely to be low, of the order of 0.1 dex.

4.5 SFR from optical lines and SED fitting

SFR can be derived from the H α and H β lines. Several conversions are possible, depending on the available data and physical condition of the galaxies. Similar to what is often done by many authors (e.g., Erb et al. 2006a; Förster Schreiber et al. 2009), we have used the ‘‘classical’’ conversion factor by Kennicutt (1998), scaling down the results by a factor 1.7 (Pozzetti et al. 2007) to convert

Table 3. Properties of the target galaxies

(1) Object	(2) $\log(M^*/M_\odot)$	(3) $A_{V,c}$ range	(4) SFR_{em} (M_\odot/yr)	(5) $r_{1/2}$ (kpc)	(6) $12+\lg(\text{O}/\text{H})$	(7) $\lg(M_{gas}/M_\odot)$	(8) f_g	(9) $\lg(y_{eff})$
SSA22a-C30	$10.33^{+0.31}_{-0.38}$	0.0–0.8	29^{+81}_{-21}	1.48 ± 0.44	$8.16^{+0.20}_{-0.60}$	9.66 ± 0.41	$0.18^{+0.26}_{-0.12}$	$-2.63^{+0.2+0.3}_{-0.2+0.1}$
SSA22a-C6	$9.68^{+0.15}_{-0.06}$	0.3–0.5	23^{+11}_{-8}	1.75 ± 0.22	$7.95^{+0.20}_{-0.50}$	9.96 ± 0.13	$0.66^{+0.08}_{-0.12}$	$-2.22^{+0.2+0.2}_{-0.4+0.2}$
SSA22a-M4	$9.41^{+0.34}_{-0.13}$	0.0–0.8	20^{+40}_{-13}	2.01 ± 0.27	$8.12^{+0.25}_{-0.45}$	9.96 ± 0.34	$0.78^{+0.12}_{-0.28}$	$-1.84^{+0.2+0.4}_{-0.4+0.4}$
SSA22b-C5	$8.96^{+0.38}_{-0.22}$	0.0–0.5	15^{+15}_{-8}	1.28 ± 0.38	$7.66^{+0.20}_{-0.20}$	9.64 ± 0.21	$0.83^{+0.08}_{-0.19}$	$-2.17^{+0.2+0.3}_{-0.2+0.4}$
DSF22-D28	$9.78^{+0.28}_{-0.29}$	0.0–0.6	14^{+18}_{-8}	1.50 ± 0.48	$8.20^{+0.10}_{-0.25}$	9.62 ± 0.25	$0.61^{+0.21}_{-0.20}$	$-2.32^{+0.1+0.3}_{-0.2+0.2}$
DSF22-MD19	$10.06^{+0.33}_{-0.27}$	0.0–1.2	39^{+77}_{-26}	2.00 ± 0.55	–	9.98 ± 0.33	$0.69^{+0.25}_{-0.26}$	–
Q0302-C131	$10.09^{+0.10}_{-0.10}$	0.0–0.3	10^{+6}_{-4}	1.27 ± 0.37	$8.00^{+0.25}_{-0.40}$	9.57 ± 0.14	$0.42^{+0.13}_{-0.07}$	$-2.73^{+0.2+0.2}_{-0.4+0.1}$
Q0302-M80	$10.07^{+0.23}_{-0.19}$	0.0–0.6	13^{+17}_{-8}	0.75 ± 0.24	$8.36^{+0.15}_{-0.15}$	9.54 ± 0.25	$0.36^{+0.16}_{-0.12}$	$-2.37^{+0.1+0.2}_{-0.1+0.2}$
Q0302-C171	$10.06^{+0.10}_{-0.28}$	0.0–0.2	5^{+2}_{-2}	1.25 ± 0.39	$8.14^{+0.25}_{-0.45}$	9.26 ± 0.11	$0.30^{+0.08}_{-0.04}$	$-2.71^{+0.2+0.1}_{-0.4+0.1}$

Columns. (2-3) Stellar mass and dust extinction from SED fitting; (4): **total SFR from emission lines**; (5): **half-light radius of line emission**; (6): gas-phase metallicity (7-8): gas mass and gas fraction; (9): effective yields; the first error is due to metallicity, the second one to gas fraction

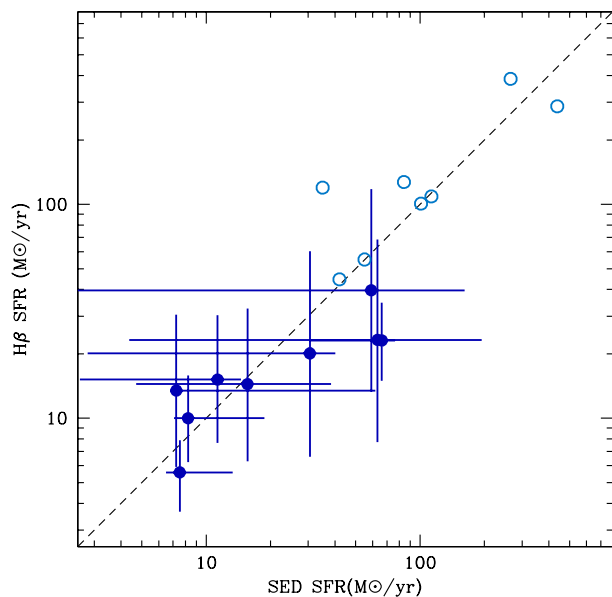


Figure 3. Comparison between the SFRs derived from SED fitting and line emission. Solid and empty dots show LSD and AMAZE galaxies, respectively. The dashed line shows equal SFRs. A good agreement is found between the two estimates of the SFR.

them to the Chabrier (2003) IMF. The Kennicutt (1998) conversion factor is based on the $H\beta$ flux corrected for dust extinction, and therefore requires a good knowledge of the amount of extinction $A_{V,el}$ suffered by the emission lines. Calzetti et al. (2000) found that this is proportional to the extinction suffered by the continuum $A_{V,c}$, as measured by SED fitting, with $A_{V,el} = A_{V,c}/0.44$ (see also Förster Schreiber et al. 2009), and here we have used this assumption. For DSF2237b-D28 the $H\beta$ flux is derived from $[\text{OIII}]\lambda 5007$ and the expected line ratio for the value of metallicity measured in the next section. The values of SFRs are listed in Table 3 and plotted in Fig. 3.

As explained in the previous section, large ranges of

extinction are allowed by our SED fitting, therefore the resulting SFRs have large errors, with typical uncertainties of one order of magnitude. This is common to most of the studies of high-redshift star-forming galaxies, even if sometimes the errors on the SFR are not accurately discussed. Unfortunately, other possible conversion factors that could provide smaller uncertainties cannot be applied to high-redshift starburst galaxies. For example, several other estimates have been proposed by Argence & Lamareille (2008), Moustakas et al. (2006) and Weiner et al. (2007), based on a combination of two emission lines (such as $[\text{OII}]\lambda 3727$ and $H\beta$), on lines and broad-band photometry, or line flux with no correction for dust extinction. These recipes are based on the empirical correlation among mass, SFR, dust extinction, luminosity and metallicity observed in local galaxies, and it is not possible to apply them for galaxies with very different properties.

The SFR derived from the emission lines can be compared with the value resulting from the fit of the SED (see Fig. 3). Large uncertainties are present due to the errors on $H\beta$ flux, the uncertainties in dust extinction correction for both estimates of SFR, the intrinsic spread of both calibrations. Nevertheless a good agreement is seen between the two estimators of the SFR.

4.6 Metallicity

Gas-phase metallicities were derived by comparing the observed line ratios with the calibrations in Nagao et al. (2006) and Maiolino et al. (2008). Metallicities are derived by a simultaneous fit of all the available line ratios, as explained in Maiolino et al. (2008). Both the uncertainties in the observed line ratios and the spread of the calibration were considered, and in some cases the latter is the dominant contribution to the metallicity error. In practice, the result is dominated by the R23 indicator or, similarly, by the $[\text{OIII}]\lambda 5007/H\beta$ ratio, while the $[\text{OIII}]\lambda 5007/[\text{OII}]\lambda 3727$ ratio is used to discriminate between the two possible branches at low- and high-metallicity. The $[\text{NeIII}]\lambda 3869/[\text{OII}]\lambda 3727$ line ratio is also a sensitive indicator, when both lines are detected. The uncertainties on metallicity are of the order of 0.2–0.3 dex, and tend to be larger when the metal-

licity has values $12 + \log(\text{O}/\text{H}) \sim 8$, when both R23 and $[\text{OIII}]\lambda 4958, 5007/\text{H}\beta$ have a maximum. In this case a small uncertainty in the line ratio produces a large uncertainty in metallicity. The results are listed in Table 3. LSD galaxies show metallicities about 10%–50% solar, similar to the values found by Pettini et al. (2001) for a different sample of LBGs at $z \sim 3$.

Dust extinction is not strongly affecting the results as the only extinction-sensitive line ratio is $[\text{OIII}]\lambda 5007/[\text{OII}]\lambda 3727$. This effect can be clearly seen in Figure 6 of Maiolino et al. (2008), showing that metallicity is barely dependent on extinction and, as a consequence, the observed line ratios leave extinction basically unconstrained. For this reason we have chosen to limit the extinction to be within the range allowed by the SED fitting. Leaving extinction totally unconstrained does not affect the best-fitting value of metallicity but only the range of confidence.

5 NOTES ON INDIVIDUAL OBJECTS

5.1 SSA22a-C30

This is the galaxy with the largest stellar mass. While $\text{H}\beta$ and $[\text{OIII}]\lambda 5007$ are in clean parts of the atmospheric spectrum, $[\text{OII}]\lambda 3727$ and $[\text{OIII}]\lambda 4958$ are affected by OH lines. $[\text{OIII}]\lambda 5007$ emission is characterized by the presence of a secondary peak, about $1''$ apart from the main one. Other lower-luminosity peaks can be present in between, although with lower significance. As a result, the object has a complex, very disturbed morphology. In the ground-based UV image, this galaxy appears less disturbed. It is elongated as the line-emitting blobs and can comprise them all.

5.2 SSA22a-C6 and SSA22a-M4

This is a pair of interacting galaxies at a projected distance of about $2''$ and with velocity difference of about 300 km/sec. All lines, except $[\text{NeIII}]\lambda 3869$, fall far from the OH atmospheric lines, allowing for a good measurement of the metallicity. C6, the southernmost object, is the brightest member both in UV and in line emission. It has an elongated structure in the UV, and also the line image shows some secondary peaks coincident with the UV elongation. M4 is compact in both UV and line images.

5.3 SSA22b-C5

This is the object with the smallest stellar mass, the only one with $\log(M_*/M_\odot) < 9$. While $[\text{OIII}]\lambda 4958, 5007$ are well detected, $[\text{OII}]\lambda 3727$ is hidden by a sky line. A marginally significant structure is detected near the expected position of the $[\text{NeIII}]\lambda 3869$ line, providing a value of the redshift ($z=3.116$) slightly larger than the value from the $[\text{OIII}]\lambda 5007$ line ($z=3.112$). This could be a real detection of the $[\text{NeIII}]\lambda 3869$ line, but both the low statistical significance and the small velocity offset make it quite uncertain. Here we assume that this is not a real line and do not use it to derive metallicity. The galaxy shape is regular and almost circular, with no significant structure around the main core.

5.4 DSF22b-D28

The line image is characterized by a compact nucleus surrounded by an extended faint emission, with a size much more compact than in the broad-band image. Its emission lines are quite faint and $\text{H}\beta$ is not detected.

5.5 DSF22b-MD19

This is the galaxy of our sample with the lowest redshift, $z=2.616$, and it is the only one where $\text{H}\alpha$ can be observed. This line falls in the K band at $2.37\mu\text{m}$, where the thermal contribution to the background is significant. Nevertheless, it is very well detected. The nearby $[\text{NII}]$ lines are not detected and we can put a limit to their flux ratio with $\text{H}\alpha$ of $[\text{NII}]\lambda 6583/\text{H}\alpha < 0.3$. Such a value excludes that the ionization could be dominated by an AGN. The $[\text{OII}]\lambda 3727$ line is outside the observed range and the $[\text{OIII}]\lambda 5007$ line is barely detected as it is coincident with a sky line. As a consequence we cannot measure the metallicity of this object. $\text{H}\beta$ is well detected in a clean part of the spectrum, and the $\text{H}\alpha/\text{H}\beta$ ratio is 4.9 ± 1.5 , significantly above the case-B value of 2.85. Assuming that this difference is due to a screen of dust following the Cardelli et al. (1989) extinction law, we derive $A_{V,el} = 1.7$. This is consistent with what is derived by the spectral fitting, $A_{V,c} = 1.1$. MD19 is very extended both in UV and in $\text{H}\alpha$. The stellar continuum of this object is clearly detected and appears to be displaced from the peak of the lines.

5.6 Q0302-C131

This galaxy is elongated both in line and UV images, with a shape reminding a classical edge-on disk. The position angle of the elongation in the line image is fully consistent with that in the UV image. Most of the lines are in a clean part of the spectrum, only the $[\text{NeIII}]\lambda 3869$ line is hidden by a sky line.

5.7 Q0302-M80

In the broad-band image this galaxy is very extended, with an elongated structure. In contrast, the line image appears very compact and regular. Both $[\text{OII}]\lambda 3727$ and $[\text{NeIII}]\lambda 3869$ fall near bright sky lines and cannot be detected.

5.8 Q0302-C171

This is the object with the faintest $[\text{OIII}]\lambda 5007$. While most of the main emission lines are not strongly affected by sky lines, the flux of $[\text{OII}]\lambda 3727$ is very uncertain because the line falls near a bright sky line at $1.613\mu\text{m}$.

5.9 Composite spectrum

The average spectral properties of the LSD galaxies can be better shown by constructing an average spectrum. Also, fainter spectral features, below detection in any single spectrum, could be revealed by summing up all the spectra. Fig. 4 shows the average, composite spectrum of

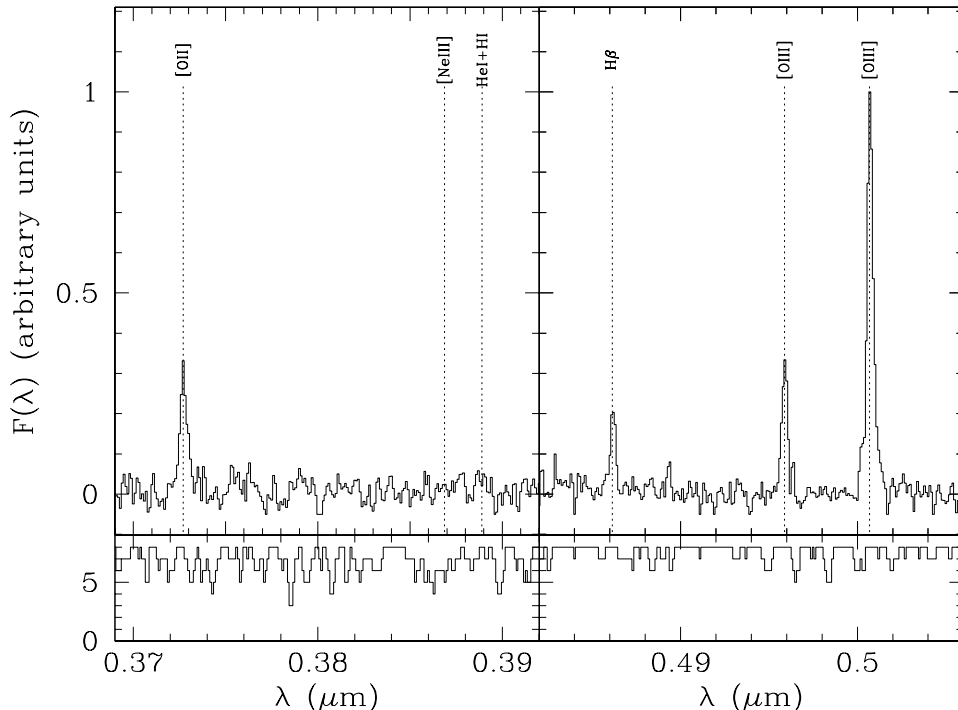


Figure 4. Composite spectrum obtained by averaging the spectra of the 8 targets covering the spectral range between [OII] λ 3727 and [OIII] λ 5007. The lower panel shows the number of spectra used for each pixel, as the pixels interested by bright sky lines were not included. The positions of the undetected lines [NeIII] λ 3869 and HeI3889 are shown for reference.

the 8 LSD sources whose spectra cover the [OII] λ 3727–[OIII] λ 5007 region. This spectrum was obtained as an average of the original ones without any weighting, and reveals the average properties of the LSD sample as if they were observed simultaneously. Large [OIII] λ 5007/H β and [OIII] λ 5007/[OII] λ 3727 ratios relative to local galaxies are shown, and this is related to metallicity as explained in section 4.6. The corresponding average mass is $\log(M_*/M_\odot)=9.80$.

6 ANALYSIS

In the previous sections we have measured stellar mass, SFR, metallicity and size of our sample of LBGs. In this section we intend to use these parameters to derive information on the history and evolutionary state of these galaxies. We will show that mass-metallicity relation, gas masses and effective yields can provide important clues on the physical processes dominating the evolution of these objects and on the relation between these starburst and similar objects at lower redshifts.

6.1 The Mass-Metallicity relation

Figure 5 shows the stellar mass-metallicity relation at $z\sim 3.1$, compared to the same relation as measured at lower redshifts. All the presented data have been scaled to a Chabrier (2003) IMF and use the same metallicity calibration. A strong, monotonic evolution of metallicity can be seen, i.e.,

galaxies at $z\sim 3.1$ have metallicities ~ 6 times lower than galaxies of similar stellar mass in the local universe. It is worth noticing that this is not the evolution of individual galaxies, as discussed in Maiolino et al. (2008), but this is the evolution of the average metallicity of the galaxies contributing to a significant fraction of the star-formation activity at their redshifts. The observed evolution implies that galaxies with relatively high stellar masses ($\log(M/M_\odot)=9-11$) and low metallicity are already in place at $z > 3$, and this can be used to put strong constraints on the processes dominating galaxy formation.

While stellar mass, based on integrated photometry, is representative of the full galaxy, metallicity is possibly dominated by the central, brightest regions. The presence of metallicity gradients could have some influence on the observed mass-metallicity relation. These aperture effects are present at any redshift: even at $z\sim 0$, galaxy spectra from SDSS refer to the central few arcsecs of the galaxies. In most models, the central brightest part of the galaxies are also the most metal rich, therefore the use of total metallicities for our LSD galaxies is expected to produce an even larger evolution.

The effect of “downsizing” (Cowie et al. 1996) on chemical enrichment is expected to produce differential evolution related to stellar mass. Stronger evolution for low-mass galaxies is observed from $z=0$ to $z=2.2$ (see Figure 5). The observed spread of the distribution and the uncertainties on the single points still make it impossible to see if such an effect is already in place between $z=2.2$ and $z=3-4$. Con-

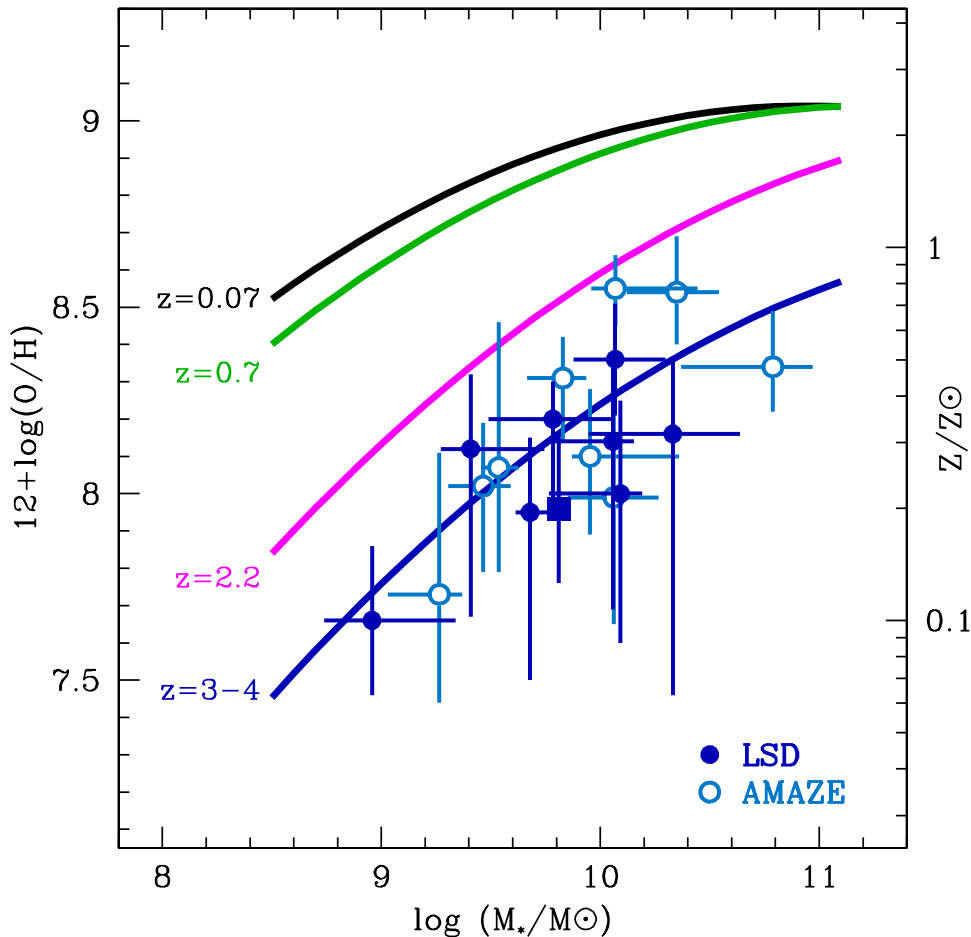


Figure 5. Evolution of the mass-metallicity relation from $z=0.07$ (Kewley & Ellison 2008), to $z=0.7$ (Savaglio et al. 2005), $z=2.2$ (Erb et al. 2006a) and $z=3-4$ (AMAZE+LSD). All data have been calibrated to the same metallicity scale and IMF (Chabrier 2003) in order to make all the different results directly comparable. Turquoise empty dots show the AMAZE galaxies, blue solid dots the LSD galaxies. The solid square shows the “average” LSD galaxy, having average mass and composite spectrum (see Figure 4). The lines show quadratic fits to the data, as described in the text.

straints on this effect can be derived when the full AMAZE data sample will be presented.

Using the same representation as in Maiolino et al. (2008), we fit the evolution of the mass-metallicity relation with a second order polynomial:

$$Z = A [\log(M_*) - \log(M_0)]^2 + K_0$$

where $A = -0.0864$ and M_0 and K_0 are the free parameters of the fit. By using the LSD and AMAZE galaxies, we derive $\log(M_0) = 12.28$ and $K_0 = 8.69$. The values of M_0 and K_0 for the samples at lower redshifts can be found in Maiolino et al. (2008), and can be converted to the present system by subtracting $\log(1.7)$ to M_0 .

Several published models of galaxy formation (e.g., de Rossi et al. 2007; Kobayashi et al. 2007) cannot account for such a strong evolution. The physical reason for this can be due to some inappropriate assumption, for example about feedback processes or merging history. When taken at face value, some other models (e.g., Brooks et al. 2007; Tornatore et al. 2007) provide a better match with the observations, but a meaningful comparison can only be ob-

tained by taking into account all the selection effects and observational biases, and by comparing not only stellar mass and metallicity but also all the other relevant parameters, such as dynamical mass, angular momentum, gas fraction, SFR, morphology and size (see, for example, Calura et al. 2009).

In fact, it is important to emphasize that the galaxy samples used for Figure 5 change with redshift. In the Tremonti et al. (2004) work, the local SDSS galaxies under study constitute an almost complete census of the local star-forming galaxies, and the derived mass-metallicity relation shows the average properties of the sample. At high redshift, especially at $z > 1$, a number of effects must be considered. Only the most active galaxies are selected, and the observed metallicity refer to these objects. If, for example, less active, already formed and enriched galaxies are present at $z=3$, they would not be present in our sample; the fraction of galaxies selected is likely to change with mass, and this is expected to introduce some systematic effect with stellar mass; the rest-frame UV selection misses extinguished galaxies, therefore an increasing fraction of dusty,

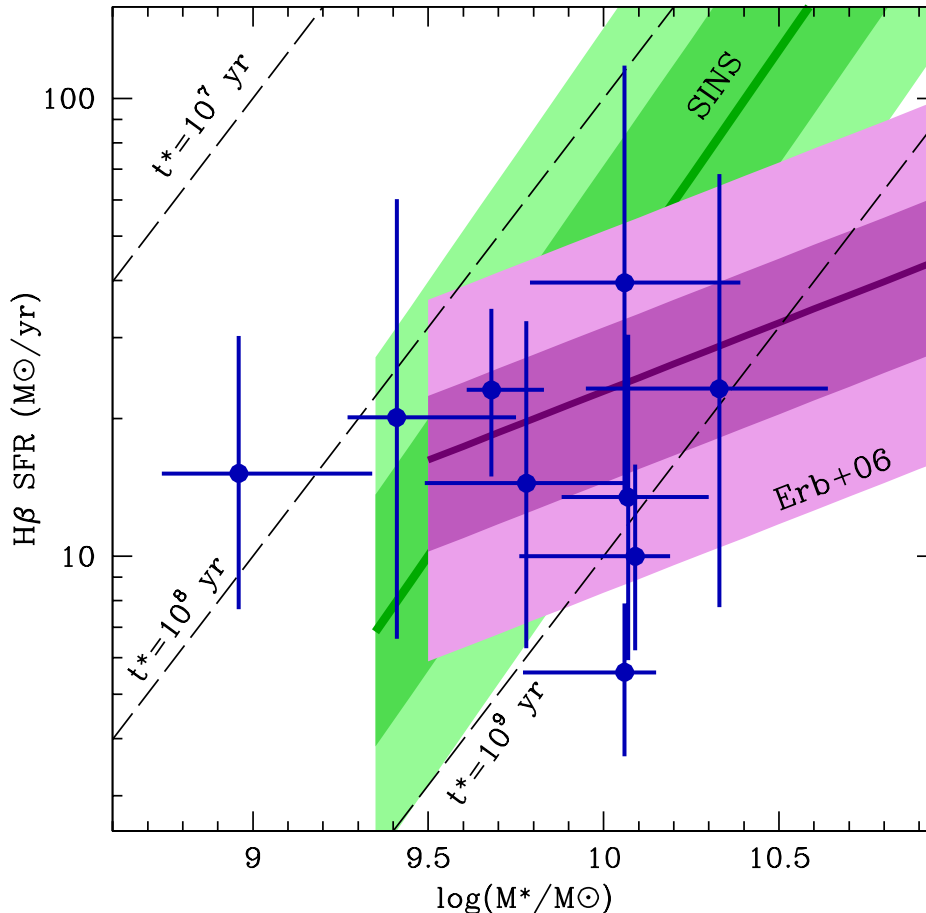


Figure 6. SFR as a function of stellar mass for the galaxies in the LSD sample. This distribution is compared with two observed correlations at lower redshift ($z \sim 2$), in magenta the UV-selected sample by Erb et al. (2006c), in green the SINS galaxies (Förster Schreiber et al. 2009). The thick lines show the median of the correlations, while the color shaded regions are delimited by the 5%, 25%, 75% and 95% percentiles of each distribution. Compared to the sample at $z \sim 2$, LSD galaxies show a larger dispersion. The long-dashed lines show some values of star formation timescales, defined as $t_* = M_*/\text{SFR}$. LSD galaxies have SF timescales between 10^8 and 10^9 yr.

metal rich galaxies are excluded from the mass-metallicity relation at high metallicities; the UGR color-color selection for the LBGs excludes galaxies with red (G–R) colors due to the presence of older stellar populations. For example, Hayashi et al. (2008) observed a sample of K-selected, star forming galaxies at $z \sim 2$. They found a mass-metallicity relation which is similar to that in Erb et al. (2006a) but with an offset of about 0.2 dex towards higher metallicities. The difference is likely to be due to target selection. Evolution in the mass-metallicity plane can also be produced by different SF histories of individual galaxies: if, for example, each galaxy experiences several bursts of star-formation, galaxies detected during the first burst will show low stellar masses and low metallicities, while galaxies with the same baryonic and total masses but detected during later bursts will show higher metallicities and stellar masses. This is not the case if galaxies have only one major burst, and all the galaxies are selected during the same phase.

All these effects are present at any redshift but their importance changes significantly among the different samples. For this reasons, the quantitative interpretation of the

observed evolution requires great care. A meaningful comparison between a sample of galaxies caught during a special phase of their life at $z=3$, with a more representative sample of galaxies at $z=0$ can only be done when the selection effects are taken into account. This will be the subject of a future work.

6.2 SFR and stellar mass

Several studies of galaxies have found a correlation between stellar mass M_* and SFR, i.e., more massive galaxies also have larger SFRs (see, for example, Schiminovich et al. 2007 for a UV-selected sample, Elbaz et al. 2007 for an optical selected sample, and Daddi et al. 2007 for a K-band selected sample). In contrast, local Ultra-luminous Infrared Galaxies (ULIRG) do not follow the same relation but lie above it (Elbaz et al. 2007). The slope of the correlation is not well constrained. While some authors (Daddi et al. 2007) find SFRs proportional to M_* , i.e., specific SFR (SSFR = SFR/M_*) constant with mass, in most cases a much weaker dependence of SFR on M_* is found (Noeske et al. 2007;

Zheng et al. 2007; Drory & Alvarez 2008). Other authors find an evolution of the slope with redshift (Dunne et al. 2008), while in some samples the SFR seems to be more directly related to stellar surface density rather than stellar mass (Franx et al. 2008).

The existence of such a relation and its slope are strongly affected by sample selection. For example, color-based selections tend to generate some proportionality between M_* and SFR because stronger SFRs are needed to significantly affect the colors of more massive galaxies. For UV-selected galaxies with SFRs estimated from the optical emission lines, similar to LSD, at $z \sim 2$ Erb et al. (2006a) have found a positive, albeit weak, correlation between M_* and SFR by removing the galaxies which have dynamical mass much higher than the stellar mass. In contrast, the SINS sample (Förster Schreiber et al. 2009) shows a much stronger dependence of SFR on M_* with slope consistent with one, in agreement with the correlation found for the K-band selected sample in Daddi et al. (2007).

To produce such a correlation, galaxies must spend a large portion of their life forming stars at a characteristic fractional level, instead of forming most of their stellar mass in a few large bursts. As a consequence, this correlation is often interpreted as an evidence that most of the star-formation activity is not related to short, intense burst but rather is associated to a more continuous activity at a lower level. This is confirmed, at $z \sim 2.2$, by the fact that the current SFR in Erb et al. (2006c) is similar to the past average. This ongoing activity could be related to cold accretion of gas followed by disk instabilities (Dekel & Birnboim 2006; Dekel et al. 2009). The regular morphologies of the galaxies dominating the star formation activity at intermediate redshifts (Bell et al. 2005; Wolf et al. 2005) and the (generally) regular dynamics observed at $z \sim 2$ (Förster Schreiber et al. 2006; Genzel et al. 2008; Shapiro et al. 2008; Stark et al. 2008) support this interpretation.

It is interesting to study if a correlation is present in our sample, and Figure 6 shows the relation between M_* and SFR in the LSD sample. Large uncertainties are present, in particular on the SFR that is very sensitive to the poorly constrained amount of dust extinction. The LSD galaxies appear to have SFRs and M_* similar to the lower-redshift galaxies in the samples mentioned above, but the small number of data points and the large intrinsic errors makes it impossible to obtain robust conclusions about the existence of a correlation.

It is important to study if selection effects could hide a strong correlation between M_* and SFR. The rest-frame UV selection explains why no galaxy below a given SFR threshold is selected. On the contrary, the lack of active, massive could be due to several effects: 1- high-mass galaxies selected as LBGs with high SFRs could be rare objects, and therefore none of them is included in this sample of 10 objects; 2- it is possible that the dust content of the galaxies increases with age and metallicity, i.e., with stellar mass. In this case massive galaxies with large SFRs could be too red or too faint in the UV to be selected as LBGs, and could be present in other catalogs as sub-mm galaxies or ULIRGs. For example, this is what is observed by Nesvadba et al. (2007) in the archetypal sub-mm galaxy SBS J14011+0252, which is both metal rich, actively star-forming, and dusty; 3- the SF activity of each galaxy could be a decreasing function of time,

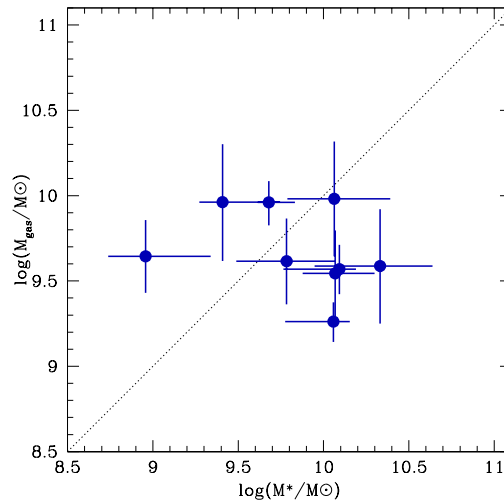


Figure 7. Mass of gas as a function of the stellar mass for the LSD galaxies. The dotted lines shows equal masses. All the galaxies have similar amount of gas, which is not related to stellar mass.

with a strong burst followed by a rapid decrease. In this case massive galaxies would also have low SFRs.

Albeit these limitations, our data do not support the existence of an almost direct proportionality ($\text{SFR} \sim M_*^{1.0}$) between SFR and M_* similar to that in Daddi et al. (2007) and Förster Schreiber et al. (2009). In contrast, we find better agreement with a flatter relation ($\text{SFR} \sim M_*^{0.3}$) as found by Erb et al. (2006a). This implies the presence of larger SSFRs in lower mass galaxies. As shown by the dashed lines in Fig. 6, the same effect can be expressed by the star-formation timescale, defined as the time t_* to form the present amount of stars M_* at the present level of SF, $t_* = M_*/\text{SFR} = 1/\text{SSFR}$. In the LSD sample, t_* changes systematically with M_* : low mass galaxies have $t_* \sim 10^8 \text{ yr}$, while higher mass galaxies have $t_* \sim 10^9 \text{ yr}$. This is an indication that, in relative terms, the current episode of star formation is more important in lower-mass systems. While high-mass galaxies have SFRs and SSFRs similar to what observed at lower redshift, low-mass galaxies tend to be relatively more active. This interpretation implies that less massive galaxies are also younger. An accurate test of this prediction is not easy, as it is difficult to measure the age of high-redshift galaxies. Nevertheless, it is consistent with the broad correlation between stellar mass and age described in sect. 4.3.

6.3 The mass in gas

In local star-forming galaxies, the surface density of star formation Σ_{SFR} is related to the surface density of gas Σ_{gas} :

$$\Sigma_{\text{SFR}} \propto \Sigma_{\text{gas}}^n$$

This is the Schmidt-Kennicutt law (see, for example, Kennicutt 1998), which seems to be already in place at high redshifts (Bouché et al. 2007). It is interesting to note that downsizing is a natural consequence of the Schmidt law and of the other scaling relations, as shown by Erb (2008). If inflows and outflows can be neglected on the timescale of

a starburst, or if they are proportional to the SFR itself, the Schmidt law produces a decreasing SFR whose initial, maximum value scales with the mass M and the size r as $M^{1.4}r^{-0.8}$, and the typical timescales as $M^{-0.4}r^{0.8}$. If we assume that galaxies follow the same mass-size relation observed in the local massive, early-type galaxies by Shen et al. (2003), we obtain that the typical timescale decreases with mass as $M^{-0.1}$ and, correspondingly, the magnitude of the initial starburst increases as $M^{1.1}$. The typical timescales computed by Erb (2008) are ~ 0.3 Gyrs for $M = 10^{12}M_{\odot}$, and ~ 4 Gyr for $M = 10^9M_{\odot}$.

The Schmidt-Kennicutt law is often used to estimate gas density and gas mass starting from the observed SFR and galaxy size (for example, Erb et al. 2006a; Erb 2008). The slope n of the relation is still uncertain. The “classic” value of n is 1.4, given by Kennicutt (1998). Star formation due to large-scale instabilities of the disk naturally produces $n=1.5$ (Elmegreen 2002), and such a value is supported by more recent observations (Kennicutt et al. 2007) on small scales. In high redshift studies, Bouché et al. (2007) found a slightly larger value, $n=1.7$, a value which depends on the adopted value of the CO/H2 ratio. Such a value could be more appropriate for our LBGs, nevertheless for consistency with previous works we adopt the relation in Kennicutt (1998), deriving the following equations for the gas surface density Σ_{gas} and the gas mass M_{gas} , valid when the Chabrier (2003) IMF is used:

$$\Sigma_{gas}(M_{\odot}/\text{pc}^2) = 254 \left(\frac{\text{SFR}}{M_{\odot}/\text{yr}} \right)^{0.71} \left(\frac{r}{\text{kpc}} \right)^{-1.42} \quad (1)$$

$$M_{gas}(M_{\odot}) = 798 \left(\frac{\text{SFR}}{M_{\odot}/\text{yr}} \right)^{0.71} \left(\frac{r}{\text{kpc}} \right)^{0.58} \quad (2)$$

Using the values in Bouché et al. (2007) would result in gas fractions about 40% lower, which however do not affect the conclusions of this work.

The largest uncertainties in these equations are related to the half-light radius r , which has large errors, as explained above. This is important for Σ_{gas} , which has a strong dependence on galaxy size. In contrast, the total gas mass M_{gas} is much less sensitive to galaxy size as it depends on $r^{0.58}$ and, as a consequence, the uncertainties on this quantity are smaller.

The observed SFR densities are between 0.5 and $6M_{\odot}/\text{yr}/\text{kpc}^2$, similar to what observed both in the local universe (Kennicutt 1998) and at $z=2.2$ (Erb et al. 2006c). The corresponding gas densities range between 300 and 2000 M_{\odot}/pc^2 , similar to the values derived for LBGs and ULIRGs by Coppin et al. (2007) and Tacconi et al. (2006). As we are sampling the central, most active part of the galaxies, these numbers must be considered as the maximum surface densities of gas.

Figure 7 shows the resulting M_{gas} as a function stellar mass. It is evident that gas mass does not correlate with M_{*} and that M_{gas} covers a much smaller range than M_{*} . While the largest galaxy has a stellar mass 24 times larger than the smallest, the most gas-rich galaxy has only 5 times more gas than the poorest. This result could be partly due to a combination of selection effects and spatial resolution. As all the galaxies have similar SFRs, the range in gas mass can be dominated by the range in intrinsic

dimensions. Our resolution, $0.2''$ FWHM, corresponding to about 1.4 kpc, is similar to the intrinsic galaxy size. As a consequence, it is possible that we are overestimating the size, and therefore the gas mass, of the smallest galaxies.

Interesting information on the physical properties of the LSD galaxies can be obtained by comparing the different timescales. We have already introduced the *stellar* timescale t_{*} , which measures the time to create the observed amount of stars at the current SFR. The typical *dynamical* timescale is $t_{dyn} = 2\pi R^{3/2}/(GM)^{1/2}$, where R is the typical radius and M the typical total mass. Any starburst activity is expected to last at least t_{dyn} (Dekel & Birnboim 2006). The LSD galaxies have t_{dyn} between 0.4 and 1.0×10^8 yr. This narrow range of values is not surprising, because if size depends on mass as in local early-type galaxies, dynamical times are almost independent of mass. A third important timescale is the *gas exhaustion* time t_{ex} , i.e., the time to exhaust all the available gas at the current rate of SF, $t_{ex} = M_{gas}/\text{SFR}$. For the LSD galaxies, this spans a narrow range, between 3 and 6×10^8 yr.

We have already seen that M_{gas}/M_{*} , and therefore t_{*}/t_{ex} , varies systematically with M_{*} , meaning that the smallest galaxies are more gas rich and are forming a larger fraction of stars. The ratio between t_{dyn} and t_{ex} ranges between 6 and 4, with no clear dependence on M_{*} . This implies that the galaxies are so gas rich that the current level of star formation can be sustained for several t_{dyn} . We cannot be sure that the SF activity will proceed for so long, but this is an indication that we are dealing with major episodes of star formation in galaxies which have accreted large amounts of gas, of the order of $10^{10}M_{\odot}$ (see Fig. 7). In these galaxies star formation follows mass assembly.

6.4 The fraction of gas

The gas mass M_{gas} can be compared with the total baryonic mass M_b to estimate the fraction of mass in gas, an indication of the evolutionary stage of the galaxy. The results are shown in Figure 8, where the gas fraction is plotted vs. the stellar mass. It should be noted that stellar and gas masses are not measured in the same apertures. When HST images for these objects are available (see sect. 3.2), we will be able to quantify this effect and apply a correction. Despite the large uncertainties, a clear correlation is seen between stellar mass and gas fraction. This is similar to what is observed at low-redshifts, where a tight correlation exists between gas fraction and rotation velocity (Dalcanton 2007) or stellar mass (Bell 2003; Kannappan 2004). The same effect is also observed by Erb et al. (2006a) and Reddy et al. (2006) in their samples at $z \sim 2$. The relation between stellar mass and gas fraction in local galaxies is often used to constrain the models of galaxy formation (e.g., Somerville et al. 2008).

The observed correlation is at least partly due to the selection effects of our target sample, shown as a grey-shaded area. As explained above, our sample is selected according to the SFR, while stellar mass can assume a wide range of values. The existence of this selection effect makes it impossible to test at $z=3$ the results of several models of galaxy formation, such as Brooks et al. (2007) and Mouchine et al.

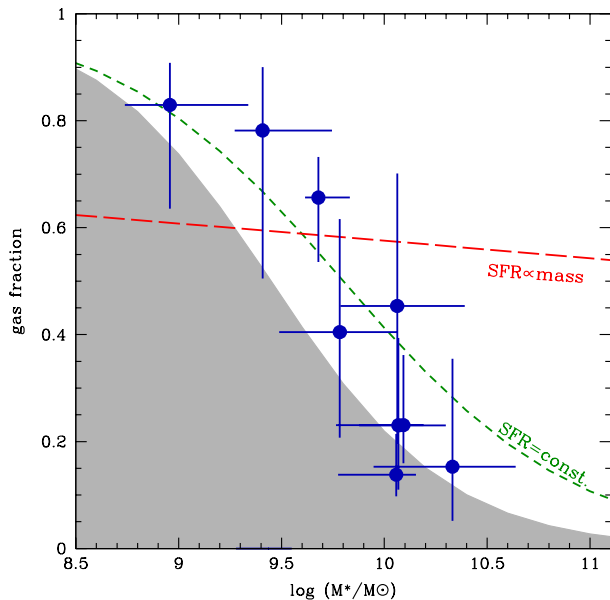


Figure 8. Fraction of baryonic mass in gas as a function of stellar mass. The blue solid dots are the LSD galaxies. The grey-shaded area represents galaxies that cannot be included in our sample because the SFR is lower than our limit ($\sim 15 M_{\odot}/\text{yr}$). The dashed lines show the expected dependence of gas fraction on stellar mass for galaxies having SFR constant (green) or proportional to the stellar mass (red).

(2008). These models predict that a strong correlation exists between f_{gas} and M_* at any redshift, with more massive galaxies having a lower content in gas, very similar to what is actually observed (see also Calura et al. 2008). In other words, the shaded region in Fig. 8 could be empty for physical reasons.

The *expected* gas fraction as a function of stellar mass can be derived once the dependence of dimensions and SFR on M_* is known. We compute this gas density using the mass-size relation for massive, late-type galaxies in Shen et al. (2003), $r \propto M^{0.4}$, and assuming that the SFR of the galaxies does not depend on stellar mass. As size are expected to change slowly with mass, these results are largely independent of the evolution of the mass-size relation, which is largely unknown. The result is plotted as a short-dashed, green line in Figure 8. In contrast, assuming that the SFR is proportional to stellar mass as observed in the local universe (see section 4.5), we derive the long-dashed, red line in the same figure. The normalization of these two lines can vary as a function of the adopted SFR and galaxy size, but the shape of the curves show that the gas fraction measured in our target galaxies is that expected for a SFR-limited sample.

6.5 The effective yields

Important hints on the physical processes shaping the mass-metallicity relation can be obtained by considering the effective yields, i.e., the amount of metals produced and retained in the ISM per unit mass of formed stars (Garnett 2002;

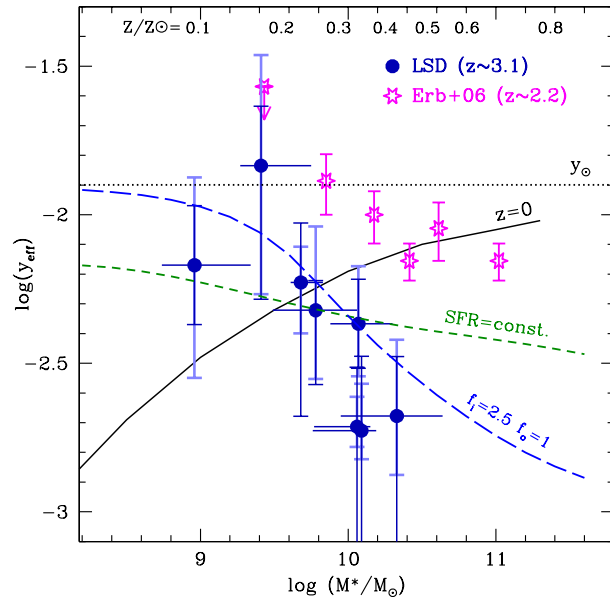


Figure 9. Effective yields of the LSD sample (solid blue dots), as a function of stellar mass, compared with the solar value (dotted line). Light and dark error bars show the contribution to the errors on yields due to the uncertainties on gas fraction and metallicity, respectively. The magenta stars are the results by Erb et al. 2006a at $z=2.2$. The black solid line are the local results by Tremonti et al. (2004). The green dashed line corresponds, as in Figure 8, to galaxies with constant SFR. The blue, long-dashed line is the model with infalls and outflows proportional to the SFR described in the text. The labels near the top of the figure show the values of the average metallicity for galaxies of a given stellar mass as derived from the mass-metallicity relation.

Dalcanton 2007). In a closed-box model, metallicity Z (i.e., the mass in metals divided by the mass of the interstellar gas) can be written as a simple function of the gas fraction f_{gas} :

$$Z = y \cdot \ln(1/f_{gas}) \quad (3)$$

where y is the true stellar yield, i.e., the ratio between the amount of metals produced and returned to the ISM and the mass of stars. This is the solution of a differential equation (see Edmunds 1990) valid in a closed-box case, with instantaneous recycling, instantaneous mixing, and low metallicities. The solar yield y_{\odot} , i.e., the fractional contribution of metals to the solar mass, is often used as reference and is 0.0126 (Asplund et al. 2004). By inverting this equation, and using observed quantities for Z and f_{gas} , we obtain the *effective* yields:

$$y_{eff} = Z / \ln(1/f_{gas}) \quad (4)$$

The measured values of y_{eff} could differ from the true stellar yields y if some of the assumptions used to derive eq. 3 do not hold, in particular if the system is not a closed box. Outflows of very enriched material, such as the ejecta from SNe, extract metals, decreasing Z , while infalls of pristine gas can increase f_{gas} and decrease Z . It is well known that both effects must be present at some level. Gas infall, either in merging episodes or in cold gas accretion, is needed to supply galaxies with the amount of matter

we observed in stars today, while starbursts are known to produce SN driven winds of the order of $0.1 M_{\odot} \text{yr}^{-1} \text{kpc}^{-2}$ (Lehnert & Heckman 1996a). The presence of both effects does not imply that both contribute significantly to the chemical evolution of the systems and, in particular, to the observed yields. In all cases, y_{eff} must be smaller than y , as discussed, for example, by Edmunds (1990) and Dalcanton (2007). This is why it is interesting to measure the effective yields, because it can measure how a system is far from being a closed-box.

In the local universe, Tremonti et al. (2004) have found a significant dependence of y_{eff} on mass, i.e., lower mass galaxies have lower y_{eff} . The reduction of y_{eff} below the solar value y_{\odot} in galaxies with low stellar mass is usually described as a consequence of outflows. If outflows are the main effect shaping the mass-metallicity relation, then the effective yields are expected to increase with stellar mass because lower mass galaxies, having a shallower potential well, have lost a larger fraction of metals into the intergalactic medium. Above a certain stellar mass, the galaxy potential well is too deep for the SNe to eject significant fraction of enriched gas, and $y_{eff} \sim y$ is expected in massive galaxies.

Figure 9 shows the values of y_{eff} for the LSD galaxies. The errors on each single point are large, as they reflect the large uncertainties on both gas fractions and metallicities. Systematic effects on dimensions could also be present, as discussed above. Nevertheless, the situation seems pretty clear: rather than *increasing* with stellar mass toward solar values, in the LSD sample y_{eff} is found to *decrease* with stellar mass, starting from y_{\odot} at the low mass end. The differences with the results by Tremonti et al. (2004) are striking. This is not surprising because it means that the physical processes dominating the SDSS galaxies in the local universe are not the same as in LBGs at $z > 3$. In contrast, our result is very similar to what has been found by Erb et al. (2006a). Our and Erb's samples share the same dependence of y_{eff} with stellar mass, although LSD galaxies have lower y_{eff} because of their lower metallicity. Our results are also similar to those of Weiner et al. (2008) at $z=1.4$ and Law et al. (2007) at $z=2.5$, who detected the presence of stronger galactic winds in more massive galaxies.

To interpret this result we have to take into account how the samples were chosen and the scaling relations. From the *expected* gas fraction in Figure 8 and the mass-metallicity relation in Figure 5, we can *predict* the y_{eff} of the LSD sample. This is a real prediction, i.e., once you define SFRs, metallicity and dimensions, there are no free parameters to compute yields. We plot this prediction in Figure 9. The observed behavior is in agreement with what is expected for a SFR-limited sample. In other words, the dependence of the yields on stellar mass is a direct consequence of the mass-metallicity relation and of the other scaling relations.

The presence of yields decreasing with mass implies that the classical outflows, whose specific power decreases with increasing galaxy mass, do not apply to the LBG at $z \sim 3.1$. The mass-metallicity relation at $z > 3$ must have a different origin.

The dependence of y_{eff} on stellar mass is a secondary effect due to the relation between stellar mass and gas fraction. For this reason, the physical meaning of these findings is better understood by plotting y_{eff} directly as a function of

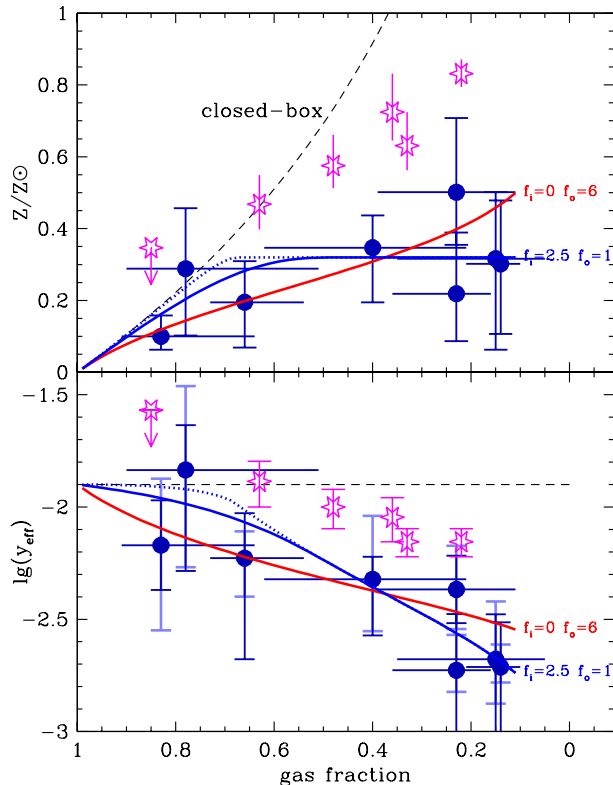


Figure 10. Metallicity (*top*) and effective yields (*bottom*) as a function of gas fraction. This is plotted decreasing rightwards, to have galaxies evolving from left to right. The blue solid dots are the LSD galaxy sample, the magenta stars the Erb et al. (2006a) data. The black dashed line shows the expectations from a closed-box model. The solid lines show the results of applying the model in Erb (2008) with values of f_i and f_o in the labels. The red line shows a model with pure outflows, with ejected mass 6 times the SFR. The blue line is a model with both infall ($f_i=2.5$) and outflow ($f_o=1$). The blue dotted line is this same model but without outflow ($f_i=2.5$ and $f_o=0$).

gas fraction. This is done in Figure 10. The relation between these two quantities and the effect of infalls and outflows are described by several authors. In particular, Dalcanton (2007) shows that outflows of very enriched materials can be very effective in reducing y_{eff} , especially for gas-rich systems. Gas-poor system can change their y_{eff} by a factor of two, as observed in the LSD galaxies, if they accrete a significant amount of gas, larger than the internal gas.

For gas rich systems, y_{eff} does not depend on f_{gas} and it is equal to the stellar yields y (Dalcanton 2007), thus allowing us to measure this quantity, which in principle could be different from y_{\odot} . Metallicity can influence nucleosynthesis in different ways. The most important effect is expected to be mass-loss, which has a strong dependence on metallicity. Massive stars with stronger stellar winds lose a larger fraction of He and C that would otherwise be converted to O. As a consequence, the oxygen yield we measure is expected to decrease with metallicity. The expected effect is not large, up to a factor of 2, but in principle measurable with our data (Woosley & Weaver 1995; Marigo 2001; Garnett 2002). All

the LSD galaxies with $f_{gas} > 0.7$ have y_{eff} fully consistent with y_{\odot} , showing that any metallicity dependence of y is not large even at $Z \sim 0.1Z_{\odot}$.

Matteucci (2001) (see also Matteucci 2008) and Erb (2008) introduce a model in which galaxies have infalls and outflows proportional to the SFR. The instant recycling and mixing approximations are used, infalling gas is assumed to have no metallicity, while the metallicity of the outflowing gas is considered to be the same as the ISM. This model can be used to reproduce y_{eff} by changing two free parameters, i.e., the amount of infall f_i and outflow f_o in unit of the SFR of the galaxy. Two more parameters can be varied, if necessary, i.e., the true yield y , and the fraction α of mass still locked in stars. Implicitly, the physical properties of these outflows differ significantly with what is invoked to explain the yields in the local universe: given the correlation between SFR and M_* (Schiminovich et al. 2007; Erb et al. 2006c), at $z \sim 2$ these outflows are expected to increase, rather than decrease, with stellar mass. Erb et al. (2006a) and Erb (2008) find that their data at $z=2.2$ can be adequately reproduced by a super-solar true yield ($y=1.5y_{\odot}$) and significant infalls and outflows, with the best-fitting parameters of $f_i=2.2$ and $f_o=1.3$.

We have applied this model to LSD, reproducing the dependence of y_{eff} on f_{gas} varying f_i and f_o . Infalls are effective in changing y_{eff} for the gas-poor galaxies, leaving gas-rich galaxies much more unaffected. Outflows are more efficient in reducing y_{eff} in gas-rich galaxies, and much less effective for gas-poor galaxies. In contrast to Erb (2008), we have fixed the values of y to y_{\odot} , as explained above. The parameter α is a slowly decreasing function of time, as more stars leave the main sequence, but can vary in quite a small range. It is expected to be ~ 0.93 at $t=10^7$ yr, ~ 0.84 at $t=10^8$ yr, ~ 0.76 at $t=10^9$ yr, and approaching 0.60–0.65 after an Hubble time (Bruzual & Charlot 2003). Given the ages of our galaxies, we have used $\alpha=0.8$, and the results are not very sensitive to the value chosen. The results are shown in Figure 10. Outflows without infalls can explain the observed y_{eff} , but in this case large values of f_o between 4 and 8 are needed. The Figure shows the best-fitting pure outflow model, having $f_o=6$. In other words, if pure outflows are responsible for the reduction of y_{eff} , the most active galaxies must eject into the IGM masses of the order of 400–800 M_{\odot} /yr, while converting 100 M_{\odot} /yr into stars. This must happen in galaxies as massive as $3 \cdot 10^{10}M_{\odot}$, i.e., galaxies that, in the local universe, show solar yields. As a comparison, Weiner et al. (2008) found outflowing masses of about 20 M_{\odot} /yr in their sample of starburst galaxies at $z=1.4$, whose SFRs are 10–100 M_{\odot} /yr, similar to the present sample. Pure infalls can explain the yields with lower amount of flowing gas. In this case, the best fitting value is $f_i=2.5$, with an acceptable range between $f_i=1.5$ and $f_i=3.5$. Once an infall with $f_i \sim 2$ is present, it dominates the behavior of y_{eff} and f_o can assume any value between 0 and 7. The best-fitting model with $f_i=2.5$ and $f_o=1$ is also plotted in Fig. 9 as a function of stellar mass, providing a good fit.

7 SUMMARY AND CONCLUSIONS: A PICTURE OF LBGs

We have obtained deep, spatially resolved, near-IR spectroscopy of a complete sample of LBGs at $z \sim 3$, selected only to be near a bright foreground star needed to drive the adaptive optics system. These galaxies are expected to give an unbiased representation of the Steidel et al. (2003) sample of LBGs. The detected optical lines give information on many aspects of these galaxies, and in this paper we have analyzed the properties related to metallicity, stellar and gas mass, and gas fraction.

A strong evolution of the mass-metallicity relation is found, i.e., LBGs at $z \sim 3$ have metallicities between 0.1 and 0.5 solar. Assuming that the Schmidt-Kennicutt law is already in place at $z \sim 3$, we derive the properties of the gas. Large masses of gas ($\sim 10^{10}M_{\odot}$) are present in these galaxies, as a result of recent episodes of gas accretion. The gas fraction is found to be anti-correlated with stellar mass, and this is possibly due to the UV selection of the sample. These results on gas mass and metallicity imply that, at these redshifts, LBGs are already massive but still metal-poor. This means that mass assembling is occurring before star formation, as observed in early-type galaxies at lower redshifts (e.g., Saracco et al. 2003, 2005; Daddi et al. 2005) Once the selection effects are accurately considered, this can be used to put constraints on the models of galaxy formation and evolution.

The time scale to produce the observed stars at the current level of star formation varies from $\sim 10^8$ yr for the smallest systems to $\sim 10^9$ yr for the galaxies with the largest stellar mass. In contrast, the timescale to exhaust the available gas is less variable, and is comparable with the dynamical times of these systems.

The effective yields decrease with stellar mass and have solar values at the low-mass end. This is in contrast with what is observed in the local universe, and can be ascribed to recent accretion of metal poor gas at a rate of the order of the current SFR. Stellar yields have solar values even at $Z \sim 0.1Z_{\odot}$.

All these evidences show that the LBGs of our sample can be described as starbursts on several dynamical timescales following major events of gas accretion, due either to gas infall or merging with gas-rich, metal poor galaxies. Low mass galaxies can be described as experiencing their first major burst of star formation. More massive galaxies are more gas poor and have lower yields, as is expected when gas infall ignites a new episode of star formation in an older galaxy. Outflows are probably present but do not dominate the chemical evolution of these systems, that is more easily driven by infalls.

These galaxies will soon be observed by HST at optical and near-IR bands. These data will complement our near-IR, spatially resolved spectroscopy in order to study the morphological and dynamical properties of these galaxies and obtain a complete picture of these LBGs.

Acknowledgments We thanks F. Eisenhauer and A. Modigliani for support during data reduction, and B. Kennicutt and T. Nagao for very useful discussions. We also thanks the staffs of ESO, Spitzer and TNG for excellent service observing, and E. Daddi for having provided data in

tabular form. This work was partially supported by the Italian Space Agency through contract ASI-INAF I/016/07/0, by INAF CRAM 1.06.09.10, and by NASA (Spitzer) grant number 1343503.

REFERENCES

- Argence, B. & Lamareille, F. 2008, ArXiv e-prints
- Asplund, M., Grevesse, N., Sauval, A. J., Allende Prieto, C., & Kiselman, D. 2004, *A&A*, 417, 751
- Baffa, C., Comoretto, G., Gennari, S., et al. 2001, *A&A*, 378, 722
- Bell, E. F. 2003, *ApJ*, 586, 794
- Bell, E. F., Papovich, C., Wolf, C., et al. 2005, *ApJ*, 625, 23
- Bolzonella, M., Miralles, J.-M., & Pelló, R. 2000, *A&A*, 363, 476
- Bonnet, H., Abuter, R., Baker, A., et al. 2004, *The Messenger*, 117, 17
- Bouché, N., Cresci, G., Davies, R., et al. 2007, *ApJ*, 671, 303
- Brinchmann, J., Pettini, M., & Charlot, S. 2008, *MNRAS*, 385, 769
- Brooks, A. M., Governato, F., Booth, C. M., et al. 2007, *ApJL*, 655, L17
- Bruzual, G. & Charlot, S. 2003, *MNRAS*, 344, 1000
- Calura, F., Jimenez, R., Panter, B., Matteucci, F., & Heavens, A. F. 2008, *ApJ*, 682, 252
- Calura, F., Pipino, A., Chiappini, C., et al. 2009, ArXiv e-prints
- Calzetti, D., Armus, L., Bohlin, R. C., et al. 2000, *ApJ*, 533, 682
- Cardelli, J. A., Clayton, G. C., & Mathis, J. S. 1989, *ApJ*, 345, 245
- Chabrier, G. 2003, *PASP*, 115, 763
- Chapman, S. C., Blain, A. W., Smail, I., & Ivison, R. J. 2005, *ApJ*, 622, 772
- Conselice, C. J., Bundy, K., Trujillo, I., et al. 2007, *MNRAS*, 381, 962
- Coppin, K. E. K., Swinbank, A. M., Neri, R., et al. 2007, *ApJ*, 665, 936
- Cowie, L. L. & Barger, A. J. 2008, *ApJ*, 686, 72
- Cowie, L. L., Songaila, A., Hu, E. M., & Cohen, J. G. 1996, *AJ*, 112, 839
- Cresci, G., Davies, R. I., Baker, A. J., & Lehnert, M. D. 2005, *A&A*, 438, 757
- Cresci, G., Hicks, E. K. S., Genzel, R., et al. 2009, ArXiv e-prints
- Daddi, E., Dickinson, M., Morrison, G., et al. 2007, *ApJ*, 670, 156
- Daddi, E., Renzini, A., Pirzkal, N., et al. 2005, *ApJ*, 626, 680
- Dalcanton, J. J. 2007, *ApJ*, 658, 941
- Davies, R. I. 2007, *MNRAS*, 375, 1099
- de Rossi, M. E., Tissera, P. B., & Scannapieco, C. 2007, *MNRAS*, 374, 323
- Dekel, A. & Birnboim, Y. 2006, *MNRAS*, 368, 2
- Dekel, A., Sari, R., & Ceverino, D. 2009, ArXiv e-prints
- Drory, N. & Alvarez, M. 2008, *ApJ*, 680, 41
- Dunne, L., Ivison, R. J., Maddox, S., et al. 2008, ArXiv e-prints
- Edmunds, M. G. 1990, *MNRAS*, 246, 678
- Eisenhauer, F., Abuter, R., Bickert, K., et al. 2003, in *Society of Photo-Optical Instrumentation Engineers (SPIE) Conference Series*, Vol. 4841, Society of Photo-Optical Instrumentation Engineers (SPIE) Conference Series, ed. M. Iye & A. F. M. Moorwood, 1548–1561
- Elbaz, D., Daddi, E., Le Borgne, D., et al. 2007, *A&A*, 468, 33
- Ellison, S. L., Patton, D. R., Simard, L., & McConnachie, A. W. 2008, *ApJL*, 672, L107
- Elmegreen, B. G. 2002, *ApJ*, 577, 206
- Erb, D. K. 2008, *ApJ*, 674, 151
- Erb, D. K., Shapley, A. E., Pettini, M., et al. 2006a, *ApJ*, 644, 813
- Erb, D. K., Steidel, C. C., Shapley, A. E., et al. 2006b, *ApJ*, 647, 128
- Erb, D. K., Steidel, C. C., Shapley, A. E., et al. 2006c, *ApJ*, 646, 107
- Fazio, G. G., Hora, J. L., Allen, L. E., et al. 2004, *ApJS*, 154, 10
- Förster Schreiber, N. M., Genzel, R., Bouche, N., et al. 2009, ArXiv e-prints
- Förster Schreiber, N. M., Genzel, R., Lehnert, M. D., et al. 2006, *ApJ*, 645, 1062
- Franx, M., Labbé, I., Rudnick, G., et al. 2003, *ApJL*, 587, L79
- Franx, M., van Dokkum, P. G., Schreiber, N. M. F., et al. 2008, *ApJ*, 688, 770
- Frye, B., Broadhurst, T., & Benítez, N. 2002, *ApJ*, 568, 558
- Gallazzi, A., Charlot, S., Brinchmann, J., & White, S. D. M. 2006, *MNRAS*, 370, 1106
- Garnett, D. R. 2002, *ApJ*, 581, 1019
- Gavazzi, G. & Scodreggio, M. 1996, *A&A*, 312, L29
- Genzel, R., Burkert, A., Bouché, N., et al. 2008, *ApJ*, 687, 59
- Halliday, C., Daddi, E., Cimatti, A., et al. 2008, *A&A*, 479, 417
- Hayashi, M., Motohara, K., Shimasaku, K., et al. 2008, ArXiv e-prints
- Hopkins, A. M. & Beacom, J. F. 2006, *ApJ*, 651, 142
- Kannappan, S. J. 2004, *ApJL*, 611, L89
- Kennicutt, Jr., R. C. 1998, *ARAA*, 36, 189
- Kennicutt, Jr., R. C., Calzetti, D., Walter, F., et al. 2007, *ApJ*, 671, 333
- Kewley, L. J. & Ellison, S. L. 2008, *ApJ*, 681, 1183
- Kobayashi, C., Springel, V., & White, S. D. M. 2007, *MNRAS*, 376, 1465
- Kobulnicky, H. A. & Koo, D. C. 2000, *ApJ*, 545, 712
- Koopmans, L. V. E. & Treu, T. 2003, ArXiv Astrophysics e-prints
- Köppen, J., Weidner, C., & Kroupa, P. 2007, *MNRAS*, 375, 673
- Lamareille, F., Brinchmann, J., Contini, T., et al. 2008, ArXiv e-prints
- Law, D. R., Steidel, C. C., Erb, D. K., et al. 2007, *ApJ*, 656, 1
- Lee, H., Skillman, E. D., Cannon, J. M., et al. 2006, *ApJ*, 647, 970
- Lehnert, M. D. & Heckman, T. M. 1996a, *ApJ*, 462, 651
- Lehnert, M. D. & Heckman, T. M. 1996b, *ApJ*, 472, 546

- Lequeux, J., Peimbert, M., Rayo, J. F., Serrano, A., & Torres-Peimbert, S. 1979, *A&A*, 80, 155
- Liu, X., Shapley, A. E., Coil, A. L., Brinchmann, J., & Ma, C.-P. 2008, *ApJ*, 678, 758
- Maier, C., Lilly, S. J., Carollo, C. M., et al. 2006, *ApJ*, 639, 858
- Maiolino, R., Nagao, T., Grazian, A., et al. 2008, *A&A*, 488, 463
- Mannucci, F., Buttery, H., Maiolino, R., Marconi, A., & Pozzetti, L. 2007, *A&A*, 461, 423
- Mannucci, F., Pozzetti, L., Thompson, D., et al. 2002, *MNRAS*, 329, L57
- Maraston, C. 2005, *MNRAS*, 362, 799
- Marigo, P. 2001, *A&A*, 370, 194
- Matteucci, F. 2001, *Astrophysics and Space Science Library*, Vol. 253, *The chemical evolution of the Galaxy* (Kluwer)
- Matteucci, F. 2008, *ArXiv e-prints*
- Michel-Dansac, L., Lambas, D. G., Alonso, M. S., & Tissera, P. 2008, *MNRAS*, 386, L82
- Modigliani, A., Hummel, W., Abuter, R., et al. 2007, *ArXiv Astrophysics e-prints*
- Mori, M., Umemura, M., & Ferrara, A. 2004, *ApJL*, 613, L97
- Mouchine, M., Gibson, B. K., Renda, A., & Kawata, D. 2008, *ArXiv e-prints*
- Moustakas, J., Kennicutt, Jr., R. C., & Tremonti, C. A. 2006, *ApJ*, 642, 775
- Nagao, T., Maiolino, R., & Marconi, A. 2006, *A&A*, 459, 85
- Nesvadba, N. P. H., Lehnert, M. D., Eisenhauer, F., et al. 2006, *ApJ*, 650, 661
- Nesvadba, N. P. H., Lehnert, M. D., Genzel, R., et al. 2007, *ApJ*, 657, 725
- Noeske, K. G., Faber, S. M., Weiner, B. J., et al. 2007, *ApJL*, 660, L47
- Panter, B., Jimenez, R., Heavens, A. F., & Charlot, S. 2008, *MNRAS*, 391, 1117
- Pérez-González, P. G., Gil de Paz, A., Zamorano, J., et al. 2003, *MNRAS*, 338, 525
- Perez-Montero, E., Contini, T., Lamareille, F., et al. 2008, *ArXiv e-prints*
- Pettini, M., Rix, S. A., Steidel, C. C., et al. 2002, *ApJ*, 569, 742
- Pettini, M., Shapley, A. E., Steidel, C. C., et al. 2001, *ApJ*, 554, 981
- Pilyugin, L. S., Vílchez, J. M., & Contini, T. 2004, *A&A*, 425, 849
- Pozzetti, L., Bolzonella, M., Lamareille, F., et al. 2007, *A&A*, 474, 443
- Reddy, N. A., Steidel, C. C., Fadda, D., et al. 2006, *ApJ*, 644, 792
- Rodrigues, M., Hammer, F., Flores, H., et al. 2008, *A&A*, 492, 371
- Saracco, P., Longhetti, M., Severgnini, P., et al. 2005, *MNRAS*, 357, L40
- Saracco, P., Longhetti, M., Severgnini, P., et al. 2003, *A&A*, 398, 127
- Savaglio, S., Glazebrook, K., Le Borgne, D., et al. 2005, *ApJ*, 635, 260
- Scannapieco, C., Tissera, P. B., White, S. D. M., & Springel, V. 2008, *MNRAS*, 389, 1137
- Schimminovich, D., Wyder, T. K., Martin, D. C., et al. 2007, *ApJS*, 173, 315
- Shapiro, K. L., Genzel, R., Förster Schreiber, N. M., et al. 2008, *ApJ*, 682, 231
- Shapley, A. E., Coil, A. L., Ma, C.-P., & Bundy, K. 2005, *ApJ*, 635, 1006
- Shapley, A. E., Steidel, C. C., Adelberger, K. L., et al. 2001, *ApJ*, 562, 95
- Shen, S., Mo, H. J., White, S. D. M., et al. 2003, *MNRAS*, 343, 978
- Somerville, R. S., Hopkins, P. F., Cox, T. J., Robertson, B. E., & Hernquist, L. 2008, *MNRAS*, 391, 481
- Stark, D. P., Swinbank, A. M., Ellis, R. S., et al. 2008, *Nature*, 455, 775
- Steidel, C. C., Adelberger, K. L., Shapley, A. E., et al. 2003, *ApJ*, 592, 728
- Stewart, K. R., Bullock, J. S., Wechsler, R. H., Maller, A. H., & Zentner, A. R. 2008, *ApJ*, 683, 597
- Tacconi, L. J., Neri, R., Chapman, S. C., et al. 2006, *ApJ*, 640, 228
- Teplitz, H. I., McLean, I. S., Becklin, E. E., et al. 2000, *ApJL*, 533, L65
- Tornatore, L., Borgani, S., Dolag, K., & Matteucci, F. 2007, *MNRAS*, 382, 1050
- Tremonti, C. A., Heckman, T. M., Kauffmann, G., et al. 2004, *ApJ*, 613, 898
- Weiner, B. J., Coil, A. L., Prochaska, J. X., et al. 2008, *ArXiv e-prints*
- Weiner, B. J., Papovich, C., Bundy, K., et al. 2007, *ApJL*, 660, L39
- Werner, M. W., Roellig, T. L., Low, F. J., et al. 2004, *ApJS*, 154, 1
- Wolf, C., Bell, E. F., McIntosh, D. H., et al. 2005, *ApJ*, 630, 771
- Woosley, S. E. & Weaver, T. A. 1995, *ApJS*, 101, 181
- Zheng, X. Z., Bell, E. F., Papovich, C., et al. 2007, *ApJL*, 661, L41